X-621-71-300
PREPRINT

# A THERMOSPHERE COMPOSITION MEASUREMENT USING A QUADRUPOLE MASS SPECTROMETER WITH A SIDE ENERGY FOCUSSING QUASI-OPEN ION SOURCE

HASSO B. NIEMANN
NELSON W. SPENCER
GERALD A. SCHMITT

JULY 1971



GSFC
GODDARD SPACE FLIGHT CENTER
GREENBELT, MARYLAND

X-621-71-300

# A THERMOSPHERE COMPOSITION MEASUREMENT USING A QUADRUPOLE MASS SPECTROMETER WITH A SIDE ENERGY FOCUSSING QUASI-OPEN ION SOURCE

Hasso B. Niemann
Goddard Space Flight Center
Greenbelt, Maryland

Nelson W. Spencer
Goddard Space Flight Center
Greenbelt, Maryland

Gerald A. Schmitt
University of Michigan
Ann Arbor, Michigan

July 1971

GODDARD SPACE FLIGHT CENTER
Greenbelt, Maryland

# A THERMOSPHERE COMPOSITION MEASUREMENT USING A QUADRUPOLE MASS SPECTROMETER WITH A SIDE ENERGY FOCUSSING QUASI-OPEN ION SOURCE

Hasso B. Niemann
Goddard Space Flight Center
Greenbelt, Maryland

Nelson W. Spencer
Goddard Space Flight Center
Greenbelt, Maryland

Gerald A. Schmitt
University of Michigan
Ann Arbor, Michigan

## ABSTRACT

The atomic oxygen concentration in the altitude range 130-240 km has been determined through the use of a quadrupole spectrometer with a strongly focussing ion source. The instrument is used in the Thermosphere Probe in a manner that greatly increases the proportion of measured oxygen ions that have not experienced a surface collision and permits quantitative evaluation of surface recombination and thermalization effects which inevitably enter all spectrometer determinations. The data obtained strengthen the concept that consideration of surface effects is significant in quantifying spectrometer measurements of reactive gases, and tend to be in agreement with von Zahn's recent results.

# A THERMOSPHERE COMPOSITION MEASUREMENT USING A QUADRUPOLE MASS SPECTROMETER WITH A SIDE ENERGY FOCUSSING QUASI-OPEN ION SOURCE

## 1. INTRODUCTION

The measurement of atomic oxygen by means of rockets has posed difficult instrumental problems because of the relatively undefinable but dominant gas/surface interactions experienced. At satellite altitudes where 0 greatly predominates over $0_2$, the 0 concentration can be measured relatively easily by recombination of the 0 into $0_2$ in the mass spectrometer ion source chamber. However, in the lower thermosphere, where 0 and $0_2$ coexist in delicate equilibrium, this approach is inadequate. We believe however that a satisfactory approach is one that employs a mass spectrometer that ionizes and measures a significant number of 0 atoms that have not experienced significant surface collisions in the ionization chamber. As a result, in the data analysis, a model can be used, which takes into account both particles which have and have not experienced surface interactions. In the experiment discussed in this paper, an instrument which was equipped with a quasi-open source and provided adequate side-energy focussing, and thus met the required conditions was employed. Because of the focussing, we were able to consider measurements at both near-zero and 90° angles of attack of the ion source. The system thus permitted evaluation of the relative gas/surface effects and made possible, we believe, unambiguous measurements of the atomic oxygen concentration in the thermosphere. We present the vertical profiles of the partial densities of 0, $0_2$, and $N_2$ obtained over the altitude region from 150 to 280 km. In addition, the techniques employed to analyze the data using a time-independent absorption model are discussed.

## 2. INSTRUMENTATION

In this experiment, a Thermosphere Probe (TP) instrumented with two mass spectrometers, a quadrupole and an omegatron, was launched from Wallops Island, Virginia, on August 26, 1966, to study the earth's atmospheric parameters in the altitude region between 120 to 350 km. The launch vehicle was a Nike-Tomahawk. It was launched at 14:31 EDT as one of a series of five launches scheduled to measure the extremes of the diurnal variation of atmospheric temperature and density.

The Thermosphere Probe (TP) which is launched in a clam-shell nose cone (Figure 1) and then ejected into the lower thermosphere with an end over end motion contained the quadrupole and omegatron mass spectrometers from which the data discussed herein were obtained. The spectrometers, mounted in the TP with their ion sources centered at each end, were kept in vacuum until an altitude of about 150 km was reached, where the automatic breakoff devices exposed the instruments to the ambient atmosphere. A short time later, measurements were initiated by turning on the filaments. The omegatron spectrometer was located behind an orifice in the conventional manner reported by Spencer, et al., 1965. The quadrupole mass spectrometer, however, utilized a quasi-open side energy focussing ion source to reduce the effect of gas-surface interactions on the atomic oxygen measurements. The source used was similar to that employed with the Explorer 17 mass spectrometers (Spencer and Reber, 1964; Reber and Hall, 1966) but its electrodes were made of gold plated stainless steel and the electrode potentials were adjusted for rocket flight conditions so that free streaming neutral particles could be analyzed in the mass spectrometer without energy and momentum discrimination.

A detailed view of the ion source is given in Figure 2. Electrons are emitted from a hot tungsten-rhenium filament and are accelerated by an electric field generated by a potential of about 75V applied between the top surface and the filament. A permanent magnetic field focuses the electrons, forcing them to move along an arc as indicated in the figure. Neutral gas particles are ionized by electron impact along the electron path. A positively-biased highly transparent (95 percent) repeller above the top surface, and an ion lens system below the center opening of the top surface provide an electric field which extracts ionized particles from the primary ionization region indicated in Figure 2. The lens system produces a magnified image of this region on the source base. A portion of this image is projected through the entrance aperture (marked in Figure 2 with an X) into the quadrupole analyzer section. This ion lens geometry is designed, at the expense of sensitivity, to assure that the transmission of ions resulting from ambient neutrals arriving in the source region is independent of the initial velocity and incident angle of the neutral particles entering the source region for rocket velocities up to about 2 km/sec. In this manner, neutral particles entering the ionization region directly from the stream are detected thus fulfilling the requirement that particles <u>not</u> experiencing a wall collision will be measured. Because some particles that have reacted with the walls and have been thermalized also inevitably are detected the ion source is referred to as quasi-open. The ratio of the concentration of free stream ions to thermalized ions is a strong function of the angle of attack and provides the basis for the primary analysis considerations of this paper.

The quadrupole analyzer section was operated in a 100% ion transmission mode which resulted in flat-topped mass peaks and permitted acceptable

tolerance for normal drifts of the operating voltages and frequencies. Selection of masses 40, 32, 28, and 16 was accomplished by varying the rf-oscillator frequency and keeping the rf- and dc-voltages constant. Two other modes of operation included first, a total density measurement for which the dc-voltages were disconnected from the quadrupole rods and the rf-frequency was tuned to the mass 16 value. Transmission of all ions with atomic masses above, approximately, mass 13 was thus assured. The other mode was a zero-transmission mode for ion detector calibration and noise evaluation in which the ion flow was interrupted by changing the ion lens voltage and tuning the rf-oscillator to a frequency corresponding to mass 25. The ions were detected at the end of the analyzer section with the aid of a secondary electron multiplier. A multiplier gain of $10^5$ provided adequate current sensitivity. The anode current of the multiplier, varying from $10^{-12}$ to $10^{-7}$ amperes was converted to a voltage range of 0 to 10 volts by a logarithmic electrometer amplifier.

During ejection from the nose cone the TP was caused to tumble end-over-end with a period of 2.62 sec. The quadrupole was tuned sequentially to the masses 32, 16, 28, 40, and zero for 2.8 sec each, corresponding to about 1.05 tumble periods, which permitted measurement through a complete tumble period for each species. During the zero ion current mode, the electrometer was calibrated at three current levels: $10^{-6}$ A, $10^{-9}$ A and zero current. Near apogee the sequence was lengthened to include the total current measurement.

Before flight the quadrupole spectrometer was pressure-calibrated simultaneously with four omegatrons against three Bayard-Alpert (BA) ionization gauges which had been calibrated against a McLeod gauge. The calibration with the BA gauges gave meaningful results for nitrogen and argon, but since BA

gauges generate carbon oxides and exhibit a memory effect when operated in an oxygen atmosphere, only a relative oxygen calibration between the omegatron and the quadrupole was obtained. Thus, during the oxygen calibration, the BA gauges were turned off. The contribution of dissociatively ionized oxygen to the atomic oxygen measurement was determined from the mass 16 to mass 32 current ratios. For absolute oxygen sensitivities, the ionization cross section ratios $\sigma(O_2)/\sigma(N_2)$ and $\sigma(O)/\sigma(N_2)$ (Kieffer and Dunn, 1966, and Fite and Brackmann, 1959) were used together with the experimental nitrogen sensitivity value.

The quadrupole system had two in-flight difficulties: (a) post-launch comparison with the omegatron made it apparent that the sensitivity for $N_2$ had decreased by approximately a factor of four, and (b) the rf-oscillator failed to tune to the proper frequency for mass 40. Subsequent studies in the laboratory on likely causes for the sensitivity change were (1) a change in the bias voltage of one of the ion source lenses which increases the magnification of the lens and thus decreases the sensitivity of the instrument, or (2) a change in the electron multiplier gain. The most probable cause of oscillator detuning at mass 40 was a failure of the reed relay used to change the oscillator frequency by capacitance switching.

In the subsequent analysis, it was assumed that ion source focusing was not adversely affected by the change in sensitivity and that the omegatron nitrogen measurement provided an adequate basis for establishing the level of in-flight quadrupole sensitivity.

## 3. ANALYSIS OF DATA

The tumbling motion imparted to the TP produces a periodic enhancement and rarefaction of the particle density in the ionization region of the quadrupole ion source. This is predicted qualitatively by the thermal transpiration equation for a moving gas (Schultz, et al., 1948), which applies to all closed and idealized ion sources. For the particular geometry of the quadrupole ion source, a quantitative analysis made by Niemann and Kreick (1966) applies.

During this flight the roll rate (period: 1.075 sec) and the tumble rate (period: 2.62 sec) of the TP resulted in a coning angle of 4.1 degrees. The sun-aspect sensor data and trajectory data permitted a continuous measurement of these angles, and thus the angle between the ion source normal and the velocity vector. Data were taken for 225 sec of flight time yielding 22 sets of data points for each mass. Since each mass was observed for 1.05 tumble periods, data were obtained at all available angles of attack. Figure 4a shows the envelope of the minimum and maximum angles experienced throughout the flight, and 4b shows the variation of instantaneous angles of attack with time for a short period.

Using in-flight omegatron data and published ionization cross sections, particle densities in the ionization region were calculated. The cross section ratios used in this analysis were: $\sigma(O)/\sigma(N_2) = 0.786$ (Fite and Brackmann, 1959); $\sigma(O_2)/\sigma(N_2) = 1.0$ (Kieffer and Dunn, 1966). Plots of source densities for the three gases (molecular nitrogen, molecular oxygen and atomic oxygen) versus time are shown in Figures 5, 6, and 7. In each figure, the same densities are shown for three distinct orientations: curve (a) minimum angle of attack attained during a given tumble, curve (b) 90 deg angle of attack, and curve (c) maximum angle of attack. The atomic oxygen densities were also corrected for

the contribution of dissociately and doubly ionized molecular oxygen which, because of the relatively high energy of the ionizing electrons and the strong focusing properties of the ion source, amounted to 50 percent of the indicated $0_2$ density. However, because of the rapid decrease of the ambient molecular to atomic oxygen ratio with increasing altitude, the contribution is very small over much of the higher altitude region.

To relate the measured particle density in the ionization region to the ambient particle densities, it is necessary to account rigorously for the gas dynamic characteristics of the ion source. Although the ion source is relatively "open", there are significant contributions to the density in the ionization region at some angles of attack by particles which have had surface collisions and, because of the focussing properties of the ion source, by those which have not.

In detailed consideration, four groups of particles, each group having a distinct history, constitute the instantaneous particle population of the ionization region: (a) particles which stream directly through the ionization region without having made any collision with the instrument surfaces, (b) particles which enter the ionization region after one bounce with the instrument surface, (c) particles which make multiple surface collisions before entering the ionizing region, and (d) particles which are slowly emitted from the surface of the instrument as a nearly constant background contribution. The ambient particles which have undergone surface collisions (single and multiple bounce) are further subdivided according to the nature of the surface collision; i.e., specular reflection, diffuse reflection, degree of thermalization, degree of absorption; the relative contribution of these various classes of particles are evaluated as a function of the variable speed ratio and angle of attack. Specifically, for the atomic oxygen

data reduction, a gas-surface interaction model is chosen to fit the data at the minimum angle of attack and at 90 deg angle of attack. Assuming that the absorption and recombination properties of the surfaces change slowly in time compared to the transition times of the gaseous particles, relations between the ambient particle density and the velocity and angle of attack dependent particle density in the ionizing region are obtained by integrating the Maxwell-Boltzmann velocity distribution function in velocity space over the proper limits for the geometry shown in Figure 8. The final expressions are given in Equations (3.1) through (3.5), which follow. The definitions of the terms used in these equations are:

$n_0$ = ambient particle number density,

$n_i$ = Number density of neutral particles in primary ionization region,

$T_i$ = instrument temperature,

$T_0$ = ambient neutral particle temperature,

K = permeability of the repeller screen,

$\theta_1$ = acute angle between the outer edge of the deck and the deck normal measured from the ion source,

$\theta_2$ = acute angle between the edge of the orifice and the deck normal measured from the ion source,

S = speed ratio, $|\vec{u}|/(2kT_0/m)^{1/2}$

where $\vec{u}$ = vehicle velocity,

k = Boltzmann's constant, $1.38 \times 10^{-23}$ J/°K,

m = molecular weight of the specie measured,

$(2kT_0/m)^{1/2}$ = most probable speed in a gas at temperature $T_0$.

$S_z$ = S cos $\alpha$,

where $\alpha$ = angle of attack between $\vec{u}$ and the deck normal.

$S_r = S \sin \alpha$,

$n_{dir}$ = contribution of particles which stream through the ionization region without collisions with the top surface prior to ionization.

$n_{spec}$ = contribution of particles which stream through the ionization region after a single collision with the top surface if all particles are specularly reflected,

$n_{diff}$ = contribution of particles which stream through the ionization region after a single collision with the top surface if all particles are diffusively reflected (according to the cosine law) without thermal accommodation,

$n_{diff,\,acc}$ = contribution of particles which stream through the ionization region after a single collision with the top surface if all particles are diffusively reflected with thermal accommodation to the temperature of the surface,

$n_{orif}$ = contribution of particles which stream through the ionization region after many collisions with the surfaces behind the orifice. Complete thermal accommodation and an ideal cavity are assumed.

$$\frac{n_{dir}}{n_0} = \frac{K}{2}\left[1 + \operatorname{erf}(S_z) + \exp(-S_z^2)\, M_0(S_z,\theta_1) + H(S_z,S_r,\theta_1)\right], \qquad (3.1)$$

where

$$H(S_z,S_r,\theta_1) = \exp\left[-(S_z^2 + S_r^2)\right] \sum_{m=1}^{\infty} \frac{S_r^{2m}}{m!} \sum_{k=1}^{m} \sin^{2k}\theta_1\, M_k,$$

$$M_0 = \cos\theta_1 \exp\left(S_z^2 \cos^2\theta_1\right)\left[1 - \operatorname{erf}(S_z \cos\theta_1)\right],$$

$$M_1 = \left(\frac{1}{2} + S_z^2 \cos^2\theta_1\right) M_0 - S_z \cos^2\theta_1 \frac{1}{\sqrt{\pi}} ,$$

$$M_i = \frac{1}{i}\left\{\left[S_z^2 \cos^2\theta_1 + \frac{1}{2}(4i - 3)\right] M_{i-1} - \frac{1}{2}(2i - 3) M_{i-2}\right\}, \; i \geq 2.$$

$$\frac{n_{spec}}{n_0} = \frac{K}{2}\left\{\exp(-S_z^2)\left[M_0(-S_z,\theta_2) - M_0(-S_z,\theta_1)\right] + H(-S_z,S_r,\theta_2) - H(-S_z,S_r,\theta_1)\right\} . \tag{3.2}$$

$$\frac{n_{diff}}{n_0} = \frac{K}{2}\left[1 + \text{erf}(S_z)\right]\left[\cos\theta_2 - \cos\theta_1\right] . \tag{3.3}$$

$$\frac{n_{diff,acc}}{n_0} = \frac{K}{2}\sqrt{\frac{T_0}{T_i}}\, f(S_z)\left[\cos\theta_2 - \cos\theta_1\right] , \tag{3.4}$$

where

$$f(S_z) = \exp(-S_z^2) + \sqrt{\pi}\, S_z \left[1 + \text{erf}(S_z)\right] ,$$

$$\frac{n_{orif}}{n_0} = \frac{K}{2}\frac{T_0}{T_i} f(S_z)(1 - \cos\theta_2) . \tag{3.5}$$

If we let $F_1$ be the probability that a particle striking the top (deck) of the ion source will be absorbed, and $F_2$ be the probability that a particle entering the ion lens region through the hole in the deck will be absorbed, we can write an equation which relates the source particle density to the ambient density in terms of the surface parameters and the gas kinetic relation given above.

$$n_i = n_0\left\{\frac{n_{dir}}{n_0} + (1 - F_1)\left[a_1\frac{n_{spec}}{n_0} + a_2\frac{n_{diff}}{n_0} + a_3\frac{n_{diff,acc}}{n_0}\right] + (1 - F_2)\frac{n_{orif}}{n_0}\right\} + n_{bkg} . \tag{3.6}$$

The last term, $n_{bkg}$, is added to account for the contribution of background gases which are absorbed on the ion source surfaces during ground calibration and preparations, and are then emitted during the flight. Of the particles colliding with the deck, $a_1$ is the fraction which shows specular reflection, $a_2$ diffusive reflection without thermal accommodation, and $a_3$ diffusive reflection with thermal accommodation. These fractions depend on the species and are, therefore, different for 0, $0_2$, and $N_2$.

The assumption that the particles reflected from the deck can be classified into three distinct groups is a simplification. More realistically, particles come off the deck according to a distribution which is somewhere between specular and diffusive with a characteristic temperature lying between their original and that of the deck. For a better approximation, an additional expression is presented which combines the equations for the diffusively reflected, thermally accommodated and non-thermally accommodated particles into one equation by using a modified velocity distribution function for the reflected particles. In the derivation, it is assumed that the incoming particles lose an amount of energy to the deck which is proportional to their initial energy. The expression which replaces the surface term

$$a_1 \frac{n_{spec}}{n_0} + a_2 \frac{n_{diff}}{n_0} + a_3 \frac{n_{diff,acc}}{n_0}$$

is

$$\frac{n_{refl}(\epsilon)}{n_0} = \frac{K}{2} \frac{f(S)_z}{f(S_z')} (\cos\theta_2 - \cos\theta_1) \sqrt{1 + \epsilon\left(\frac{T_0}{T_i} - 1\right)} \left[1 + \mathrm{erf}(S_z')\right] , \quad (3.7)$$

where

$$S_z' = \sqrt{\frac{1 - \epsilon}{1 + \left(\frac{\epsilon}{1 - \epsilon}\right)\frac{T_0}{T_i}}}\, S_z \ .$$

The term $\epsilon$ is the accommodation efficiency defined:

$$\epsilon = \frac{|\vec{v}-\vec{u}|^2 - |\vec{v}'|^2}{|\vec{v}-\vec{u}|^2 - \frac{C_0^2}{C_s^2}|\vec{v}|^2}$$

where

$\vec{u}$ = probe velocity,

$\vec{v}$ = particle velocity in the stationary coordinate system,

$\vec{v}'$ = final particle velocity after collision,

$C_s = \sqrt{2kT_s/m}$, most probable speed in a gas at the temperature of the surface,

$C_0 = \sqrt{2kT_0/m}$, most probable speed in a gas at ambient temperature.

A derivation of Equation (3.7) is given in Appendix A. In the subsequent reduction of the data both models were compared.

## 3.1 Molecular Nitrogen

The ambient nitrogen density may be computed by using Equation (3.6) for any orientation provided that TP velocity, TP angle of attack, accommodation coefficients and ambient temperatures are known. The constant background contribution to the source density is eliminated by taking the differences between the output at some known angle of attack and the minimum measured output as in the omegatron experiment data analysis. Equation (3.8) takes this procedure into account and follows from Equation (3.6). Here it is assumed that the surface

reflects all particles diffusively ($a_1 = 0$), that no adsorption occurs ($F_1 = 0$, $F_2 = 0$), and that the accommodation coefficients are independent of angle of attack.

$$\Delta n_i = n_0(N_2) \left\{ \Delta \frac{n_{dir}}{n_0(N_2)} + a_2 \Delta \frac{n_{diff}}{n_0(N_2)} + (1-a_2) \Delta \frac{n_{diff,acc}}{n_0(N_2)} + \Delta \frac{n_{orif}}{n_0(N_2)} \right\} , \quad (3.8)$$

where

$\Delta n_i = n_i(\alpha) - n_i(\alpha_{max})$, etc.

$\alpha$ = chosen angle of attack

$\alpha_{max}$ = maximum angle of attack.

The ambient nitrogen density may also be computed from Equation (3.9) in which Equation (3.7) is used to estimate surface contributions to the ion source density.

$$\Delta n_i = n_0(N_2) \left\{ \Delta \frac{n_{dir}}{n_0(N_2)} + \Delta \frac{n_{refl}}{n_0(N_2)} (\epsilon) + \Delta \frac{n_{orif}}{n_0(N_2)} \right\} . \quad (3.9)$$

The computed source density-to-ambient density ratio depends on the ambient gas temperature which during this experiment was measured by the omegatron. The uncertainty in the thermal accommodation parameter can be reduced by applying Equation (3.8) at different angles of attack since the angular dependence of each term in Equation (3.8) is different. A suitable second determination of the accommodation coefficient is obtained when the angle of attack is 90 degrees, where the direct-streaming contribution is relatively large, and all the terms in Equation (3.8) or (3.9) depend only weakly on the ambient temperature. Again, the differences between these readings and the readings at the maximum angle of attack were used to eliminate the background.

Equation (3.8) was used to solve for the ambient nitrogen density, $n_0$, by using the given parameters and the measured source densities from both upleg and downleg data, using source densities at different angles of attack. Unknown parameters, namely, accommodation coefficients and ambient temperatures, were determined by requiring that all calculations be consistent with a unique ambient density profile. To determine the accommodation coefficients of nitrogen on the quadrupole ion source deck, the following approach was used.

An ambient profile was calculated for each of two extreme assumptions of (a) complete thermal accommodation of the particles to the deck, and (b) zero thermal accommodation. Calculations for both minimum angle of attack and 90 deg angle of attack were made. In this manner, four upleg density profiles for differing conditions were obtained, which are plotted in Figure 9. The same procedure was followed to obtain density profiles using the downleg data.

A single density profile estimate was then determined from the four cases by assuming accommodation coefficients which were (a) constant for the entire measurement period, and (b) resulted in closest agreement between the available calculated profiles. The resulting single profile is shown in Figure 10, and corresponds to coefficients $a_2 = 0.56$ and $a_3 = 0.44$. By using the accommodation efficiency correlation with $\epsilon = 0.52$, employed in Equation (3.7), a separate set of data were computed which are also shown in Figure 10. These data differ little from those resulting from use of the coefficients $a_2$ and $a_3$.

The downleg data obtained at 90 deg angle of attack yielded ambient densities in exact agreement with the upleg results. However, the downleg data obtained from measurements at minimum angle of attack yielded ambient density values

approximately 20% higher than the upleg values. It was concluded that a linear scale adjustment to force these data points to coincide with the rest was appropriate, as will be discussed later in the paper.

### 3.2 Molecular Oxygen

The molecular oxygen data reduction procedure is similar to that followed for nitrogen. The computations are more complicated, however, because molecular oxygen exists also on the surface of the instrument due to recombination of atmospheric atomic oxygen. To separate the contribution of the atmospheric molecular oxygen and the recombined atomic oxygen, atomic recombination must be taken into consideration. The expression for the total source (oxygen) density is:

$$\Delta n_i(O_2) = n_0(O_2) \left\{ \Delta \frac{n_{dir}}{n_0(O_2)} + a'_2 \, \Delta \frac{n_{diff}}{n_0(O_2)} + (1-a'_2) \, \Delta \frac{n_{diff,acc}}{n_0(O_2)} + \Delta \frac{n_{orif}}{n_0(O_2)} \right\} \tag{3.10}$$

$$+ n_0(0) \left\{ \frac{\gamma}{2} \left[ a''_2 \, \Delta \frac{n_{diff}}{n_0(0)} + (1-a''_2) \, \Delta \frac{n_{diff}}{n_0(0)} \right] + \frac{1-R}{2} \, \Delta \frac{n_{orif}}{n_0(0)} \right\},$$

where $\gamma$ denotes the probability of recombination after one collision and generally depends upon particle flux, and R is the fraction of recombined atomic oxygen exiting the ion lens region given by:

$$R = \frac{1}{1 + \frac{\gamma}{p(1-\gamma)}}$$

p is the probability of escape from the ion lens region after a collision, which is assumed to be the same after each collision (Niemann and Kreick, 1966). The

primes on accommodation coefficients denote the different degrees of accommodation involved for atomic and molecular oxygen.

From these expressions, density profiles were computed for the extreme cases of complete thermal accommodation and of zero thermal accommodation. Several values of $\gamma$ and R were tried, but only those profiles resulting from the assumption of zero recombination of atomic oxygen had the proper altitude dependence for diffusive equilibrium. At higher altitudes, even a very low recombination rate would have been apparent in the molecular oxygen measurement because of the high $0/0_2$ ratio. It was concluded therefore that during the time of measurement, the atomic oxygen was either absorbed, reflected, or possibly formed another constituent by reacting with some contaminant which was adsorbed on the surfaces. The upleg results of the ambient density computation similarly without atomic oxygen recombination are shown in Figure 11.

The choice of the coefficients $a_2 = 0.21$ and $a_3 = 0.79$ for both orientations resulted in a single profile as shown in Figure 12, where downleg results are also plotted. The downleg data obtained from minimum angle of attack measurements also showed values which were 20% higher than the data obtained for the upleg and 90° angle of attack measurements. A scale adjustment was made for these data points on Figure 12.

### 3.3 Atomic Oxygen

The analysis of atomic oxygen data is more complex because of the stronger chemical reactions it experiences with the ion source surfaces. Oxygen atoms can react in several ways with the instrument surface, the most probable reactions appearing to be atomic recombination, permanent adsorption, and the

formation of gaseous constituents by reaction with previously adsorbed gases. Laboratory simulations of flight experiments and direct flight tests with omegatron mass spectrometers have shown that atomic oxygen is strongly adsorbed on "clean" instrument surfaces for time periods which greatly exceed the measurement duration of this experiment. In all omegatron flight experiments of this kind, no oxygen was detected in atomic form for the sensors employed, that were constructed from either stainless steel or gold-plated stainless steel.

To analyze the atomic oxygen data measured by the quadrupole it is, therefore, necessary to consider adsorption phenomena. Since the specific surface characteristics are not well known, some simple assumptions were made to compute the extreme values of the possible ambient atomic oxygen density profiles. As in the analysis of the $0_2$ and $N_2$ data, the criterion that the assumptions made be consistent at all angles of attack again provides a powerful tool.

It was established as discussed above that in the molecular oxygen data analysis that no significant atomic oxygen recombination occurred which contributed to the molecular oxygen measurement. In the atomic oxygen analysis, therefore, it follows that there is no loss of atomic oxygen due to recombination. By using the same procedure as in the reduction of the nitrogen data the equation for the source density difference is obtained.

$$\Delta n_i(0) = n_0(0) \left\{ \Delta \frac{n_{dir}}{n_0(0)} + (1 - b_2) a_2 \Delta \frac{n_{diff}}{n_0(0)} \right. \tag{3.11}$$

$$\left. + (1 - b_3) a_3 \Delta \frac{n_{diff,acc}}{n_0(0)} + (1 - b_4) R \Delta \frac{n_{orif}}{n_0(0)} \right\},$$

where $b_2$, $b_3$, and $b_4$ are numbers equal to or smaller than unity. These numbers allow for fractional adsorption and the loss of atomic oxygen due to reactions on the surfaces to be included in the gas-dynamics model. Based on the results of the omegatron experiments, it is assumed that the particle contribution of the atomic oxygen streaming back out of the orifice to the ionizing region was negligible and that only direct streaming particles, and particles reflected from the top deck contributed to the atomic oxygen source density. This assumption required that $b_4 = 1$, so Equation (3.11) becomes

$$n_i(0) = n_0(0) \left\{ \Delta \frac{n_{dir}}{n_0(0)} + a_2(1-b_2)\, \Delta \frac{n_{diff}}{n_0(0)} + (1-a_2)\,(1-b_3)\, \Delta \frac{n_{diff,acc}}{n_0(0)} \right\} . \quad (3.12)$$

The upleg ambient atomic oxygen density was computed using this equation for three extreme cases: (a) total adsorption on the deck ($b_2 = b_3 = 1$), (b) no adsorption or recombination on the deck with all particles reflected diffusively (zero accommodation), and (c) no adsorption or recombination on the deck with all particles reflected diffusively after complete thermal accommodation. The resulting six density profiles for minimum angle of attack and for the 90 deg angle of attack are shown in Figures 13 and 14. Again, to bring the minimum angle of attack results and the 90-deg angle of attack results into agreement, the coefficients were adjusted.

Considering these results in contrast to the cases of nitrogen and molecular oxygen, the slopes of the atomic oxygen profiles obtained from the 90 deg angle of attack were lower than the slopes of the minimum angle of attack profiles. Solving for the accommodation coefficients (assuming they were constant) yielded close, but still unacceptable, agreement for the cases of no adsorption and full

thermal accommodation. This profile was essentially identical to profile C in Figure 13. The slope of this curve, however, was considerably less than that required by assuming thermal and diffusive equilibrium of the atmospheric atomic oxygen.

As noted before, in a closed source where many wall collisions occur, atomic oxygen is completely adsorbed by gold plated stainless steel walls during the period of a rocket flight. However, the probability of adsorption after one bounce is unknown. Assuming that the ambient atomic oxygen was in thermal and diffusive equilibrium, a density profile was computed with an arbitrary magnitude but with a slope which corresponded to the ambient temperature obtained from the accompanying omegatron experiment. This theoretical profile was compared to the profile obtained from the measured data and the disagreement between them was attributed to surface sorption and possibly atomic recombination forming compounds other than molecular oxygen. To be physically meaningful, the theoretical density profile so determined must lie between the curves A and C of Figures 13 and 14. The spread between the curves A and C in Figure 14 is narrower than that in Figure 13, thus limiting the possible choice to that indicated by the dashed lines in Figure 14. The upper curve would be valid if total adsorption occurred at the low altitude, and the lower curve would be valid if no adsorption occurred at the high altitude extreme. The correct profile must then lie between the lines whose ordinates differ by about 16 percent.

A theoretical adsorption curve was fitted to the curves in Figures 13 and 14, and an improved ambient density profile was computed with the aid of this model. The simplest profile which could be fitted to the curves was a multilayer adsorption model derived by letting the adsorption characteristics of the first

layer of atoms on the surface be different from the characteristics of the higher order layers, and by using a steady state approximation. The derivation of this model is given in Appendix B and is similar to the Brunauer-Emmett-Teller adsorption Model (Flood, 1967). Only the final numerical expressions are given here. For the 90 deg angle of attack,

$$F_{90°} = \frac{\Gamma_1^2}{\Gamma_1^2 - (.528 \times 10^{13})\Gamma_1 + 6.89 \times 10^{26}} , \tag{3.13}$$

and for minimum angle of attack,

$$F_{\alpha_{min}} = .517 \frac{\Gamma_1^2}{\Gamma_1^2 + (3.23 \times 10^{13})\Gamma_1 + 2.00 \times 10^{26}} , \tag{3.14}$$

where $\Gamma_1$ is the incoming flux density of atomic oxygen (part/cm$^2$ sec), and F is the fraction of incoming flux that is adsorbed by the deck. The coefficients $a_2$ and $a_3$ were arbitrarily chosen to be 0 and 1 respectively for this component. An upleg ambient density profile including adsorption was computed and is shown in Figure 15. It should be noted that this procedure is not unique and that different surface adsorption models may yield similar atomic oxygen density profiles. Therefore, no conclusion about the surface reactions was drawn from this analysis.

In contrast to the upleg density profile the profiles computed from the downleg measurement had the same slope as would be expected from a gas in diffusive and thermal equilibrium. A final downleg profile was, therefore, computed by solving for the coefficient $a_2$ and $a_3$ and assuming no surface adsorption. Agreement with the upleg data was obtained by choosing the coefficients for the 90° angle of attack $a_2 = 0.34$ and $a_3 = 0.66$. The downleg shift in apparent sensitivity,

observed for the molecule species near minimum angle of attack was also found in this measurement.

## 3.4 Temperature

The kinetic temperature was determined by integrating the differential equation formed by the hydrostatic equation and the equation of the state of the ideal gas.

$$T(h) = \frac{\int_h^{h_0} \rho(h')\, g(h')\, dh'}{R\rho(h)} + \frac{\rho(h_0)}{\rho(h)}\, T(h_0) \qquad (3.15)$$

where

$g$ = gravitational acceleration

$\rho(h)$ = mass density at the particular altitude h

$h$ = altitude

$h_0$ = reference altitude where $h_0 \geq h$

$T(h)$ = neutral particle temperature at the particular altitude h

$R$ = universal gas constant (8.314 J/mole-deg).

The technique described above is essentially the same as that used to compute the temperature profile from the nitrogen density profile measured with the omegatron. All quantities in Equation (3.15) are taken from the quadrupole results except $T(h_0)$, which is taken from the omegatron data (Spencer et al., 1970). The resulting profile is shown in Figure 18. As expected, there is agreement with the nitrogen temperature profile of the omegatron. Molecular oxygen and molecular nitrogen profiles measured by the quadrupole are also consistent with an atmosphere in thermal and diffusive equilibrium, and the atomic oxygen density

profile has been constrained to yield the same temperature as that of the molecular nitrogen profile.

## 4. DISCUSSION

Before conclusions can be drawn from these data, it is necessary to discuss the errors which contribute to the uncertainty in the measurements. The errors common to the omegatron and the quadrupole experiments are those due to errors in trajectory, velocity, angle of attack, and calibration. They have been discussed by Spencer, et al. (1965), and for the particular case under consideration are expected to be as follows: maximum error due to position uncertainties is ±5 percent. The velocity uncertainty is smaller than ±1 percent, which results in a density error of about ±1 percent. The angle of attack, obtained by an optical technique using the method described by Carter (1968), is believed to be within ±5 deg, which results in a maximum error of ±10 percent at 90 deg angle of attack and less than ±2 percent at minimum angle of attack. The telemetry error is less than ±2 percent.

By far the largest uncertainty is that of the pressure calibration. Both the quadrupole and the omegatron were calibrated simultaneously on a dynamic calibration system against several Bayard-Alpert (BA) ionization gauges, used as secondary standards. The absolute accuracy was believed at the time to be approximately ±25 percent for molecular nitrogen. However, present indications, and new knowledge about MacLeod gauge trap pumping effects would lead one to increase the calibration constants by constant factor of 1.2. Absolute calibrations for molecular oxygen could not be obtained because of the memory effect of the BA gauges in an oxygen atmosphere. Also, because an adequate technique does not exist, atomic oxygen calibration could not be performed. Relative calibrations were carried out, however, for molecular oxygen and were automatic for molecular nitrogen. The relative calibration accuracy between the omegatron

and the quadrupole was considered to be within ±5 percent but, because of the change in the sensitivity of the quadrupole, this calibration was useful only for the quadrupole internally. Since the omegatron calibration is believed to be valid, all quadrupole measurements were corrected by a constant factor so that the molecular nitrogen density values for the omegatron and the quadrupole, were identical in magnitude at 239 km. The internal consistencies of the nitrogen and the molecular oxygen data and extensive checking of an identical system in the laboratory led to the conclusion that a shift in the sensitivity of the instrument occurred that could be represented by a constant. The sensitivities for atomic and molecular oxygen were computed with the aid of published ionization cross section ratios (Fite and Brachmann, 1959) (Kieffer and Dunn, 1966). The accuracy of the cross section ratios is not well known but the errors are probably not larger than ±20 percent.

No definite explanation could be found for the apparent sensitivity change which seemed to affect the data near minimum angle of attack. The most probable causes for this orientation-dependent change would be an interference between the sun and the ion source, as frequently encountered in TP experiments, or possibly an effect of the earth's magnetic field on the gain of the secondary electron multiplier. A similar but smaller gain change was observed in a laboratory test on an identical secondary electron multiplier. However, the data obtained at 90 deg angle of attack were in good agreement, both upleg and downleg, and plots of the instrument orientation with respect to the earth's magnetic field vector versus time support this argument. Near the peak, the downleg data includes a slight density increase compared with the upleg data. This deviation is clearly due to noise and telemetry interference. When the omegatron was

pointing so as to be illuminated by the sun near apogee the electrometer amplifier of the omegatron system saturated, driving the telemetry subcarrier oscillator out of band which generated interference in the adjacent quadrupole channel.

It was pointed out earlier that little data are available on gas-surface interactions which could be applied to the analysis of the quadrupole data. Thus, errors in the absolute ambient particle densities might occur because of the uncertainties in the accommodation coefficients and surface adsorption. Some of the uncertainties were eliminated by using data taken at different angles of attack (minimum and 90 deg), an approach adequate for molecular nitrogen and molecular oxygen. The computation using either the constant coefficients $a_2$ and $a_3$ or the accommodation efficiency $\epsilon$ did not yield significantly different results because these approaches were alternate ways of accounting for thermal accommodation. In the first attempts to analyze these data specularly reflected particles were included, and the results obtained were only slightly different from results obtained without specular reflections.

The atomic oxygen data required additional critical consideration, for the computations were complicated by surface adsorption. It was clear that the assumed adsorption model did not adequately represent the detailed physical processes, e.g., steady state assumption could not fully apply. The final results would be similar, however, since the final profile must fall between the extremes shown in Figures 13 and 14. Although the data obtained at the times of minimum angle of attack allowed the ambient profile to fall into a level which could be uncertain by a factor of four, the data obtained at 90 deg angle of attack permitted an uncertainty of only approximately 16 percent. This uncertainty did not depend

on the surface adsorption model which in our computations narrows the final choice only in a somewhat arbitrary way.

Finally, one might suspect that the change in slope of the ambient density profile based on 90 deg angle of attack data might point to a failure of the ion source to focus energetic particles. As expected, it is more difficult to focus particles into the analyzer section at the 90 deg angle of attack than at small angles of attack. However, a careful analysis showed that the focusing correction required to bring the ambient density profile, based on 90 deg angle of attack data, into agreement with the profile based on the minimum angle of attack data led to unrealistic assumptions about the electro-dynamic properties of the ion source, thus reinforcing our confidence in the focussing properties of the ion source. It would also have contradicted the results obtained for molecular nitrogen and molecular oxygen where no focusing correction was required but where higher particle kinetic energies were encountered. A possible change in the focusing of the ion source was therefore discarded.

The ratios of atomic oxygen density to molecular nitrogen and molecular oxygen density are higher than the values measured by some experimenters (Hedin, et al., 1964; Hedin and Nier, 1966), but lower than the values measured by Mauersberger, et al., 1968, von Zahn, 1970. The preliminary results of the recent measurement made with a liquid helium cooled ion source of Offermann and von Zahn, 1971 indicate an only slightly higher $0/0_2$ ratio when compared with extrapolated values of our data. There is, however, relatively good agreement in the total mass density versus altitude with the corresponding theoretical model of the CIRA 1965, COSPAR International Reference Atmosphere. For comparison the total mass density versus altitude was plotted in Figure 19,

together with the value of the CIRA 1965 models three and four. These results correspond to a 10.7 cm solar flux of $100 \times 10^{-22}$ $W/m^2Hz$ and $125 \times 10^{-22}$ $W/m^2Hz$ respectively. The three month average value preceding the launch data, August 26, 1966, was $103 \times 10^{-22}$ $w/m^2Hz$. The geomagnetic index $a_p$ was 6. The model values of the atomic oxygen, molecular oxygen, and molecular nitrogen densities were compared in Figure 16 with the measured values and good agreement was found between the atomic oxygen and the molecular nitrogen densities. The molecular oxygen densities were lower than predicted. Since the CIRA model was derived from the total mass density determined from the satellite drag analysis the close agreement between the present results and the model density of molecular nitrogen was striking and it represents an exception from results which were obtained for other molecular nitrogen measurements. These were consistently lower than the predicted value of the theoretical model. It is also interesting to note that the measured ambient temperatures were not in agreement with but lower than the model values, a fact which is consistent with earlier findings of the omegatron experiment.

## 5. SUMMARY AND CONCLUSIONS

We report in this paper the results of a different approach to the measurement of atomic oxygen in the lower thermosphere using a mass spectrometer. The primary advantage of the method is the capability of the mass spectrometer employed to ionize, focus and analyze a significant number of atmospheric neutral particles that have not experienced surface collisions and thus are truly representative of the ambient conditions. Because of the presence of surfaces, the relative velocity between the instrument and the atmosphere and a varying angle of attack the measurement will always involve some particles which have experienced surface collisions, the number varying strongly with angle of attack. In this particular application, the ratio of these two "classes" of particles varies substantially, thus permitting evaluation of the effects of surface collisions. A comparison is made between data taken when particles which have experienced surface collisions predominate over those which have not, and in circumstances where the opposite holds true. As a result it is possible to evaluate the degree of thermalization and the degree of absorption of the particles, two properties which have strong bearing on the interpretation of data taken during a rocket flight. These observations are consistent with the hypothesis that atomic oxygen is either completely absorbed or, at best, only partially thermalized upon impact with instrument surfaces, thus leading to higher concentrations of 0 than would be the case if one assumed complete thermalization.

The results presented here, when compared with data obtained by other workers and the assumptions they were obliged to make, seem to verify the above assertions. The measured atomic oxygen concentrations are greater, in general, than those obtained by the University of Minnesota Group of Prof. A. O.

Nier (Hedin et al., 1964, Hedin et al., 1966, Kasprzak et al., 1968, and Krankowsky et al., 1968) but are less than those measured by the University of Bonn Group of Prof. U. von Zahn (Manersbeze et al., 1968, Bitterbeg et al., 1970). At the same time, the total density compares favorably with the model atmosphere. It must be recognized that all rocket borne atomic and molecular oxygen measurements made so far provide only a random sample of a region of the atmosphere in which the composition is expected to be considerably more variable than predicted by our present atmospheric models. An accurate comparison of the various instruments to measure atomic oxygen can therefore only be obtained by either a coordinated measurement approach at the lower altitude, for example near 120 km, or by designing the instruments so that they reach an altitude where atomic oxygen is the major constituent and where the density data can be compared to satellite drag derived density values.

ACKNOWLEDGMENT

The authors wish to acknowledge the assistance of the many individuals involved in the preparation of the quadrupole mass spectrometer system and the Thermosphere Prope instrumentation system in which the quadrupole and the omegatron spectrometers were launched. In particular, the special contributions of J. Maurer, G. Carignan, J. Caldwell and P. Freed are noted.

## REFERENCES


Bitterberg, W., K. Brutchhausen, D. Offermann, and U. von Zahn, Lower thermosphere composition and density above Sardinia in October, 1967, J. Geophys. Res., 75, No. 28, 5529-5534.

Carter, M. F., The Attitude of the Thermosphere Probe, University of Michigan Scientific Report 07065-4-S, April 1968.

CIRA 1965 (COSPAR International Reference Atmosphere 1965), North-Holland Publishing Company, Amsterdam, 1965.

Fite, W. L. and R. T. Brackmann, "Ionization of Atomic Oxygen on Electron Impact," Physical Review, 113, 815-816, 1959.

Flood, E. A. (ed.), The Solid-Gas Interface, Vol. 1, Ch. 3, Marcel Dekker, Inc., New York, 1967.

Hedin, A. E., C. P. Avery, and C. D. Tschetter, "An Analysis of Spin Modulation Effects on Data Obtained with a Rocket-Borne Mass Spectrometer," Journal of Geophysical Research, 69, No. 21, 4637-4648, November 1, 1964.

Hedin, A. E. and A. O. Nier, "A Determination of the Neutral Composition, Number Density and Temperature of the Upper Atmosphere from 120 to 200 Kilometers with Rocket-Borne Mass Spectrometers," Journal of Geophysical Research, 71, 4121-4131, 1966.

Kasprzak, W. T., D. Krankowsky, and A. O. Nier, A study of day-night variations in the neutral composition of the lower thermosphere, J. Geophys. Res., 73, No. 21, 6765-6782, 1968.

Kieffer, L. J. and G. H. Dunn, "Electron Impact Ionization Cross-Section Data for Atoms, Atomic Ions, and Diatomic Molecules: I. Experimental Data," Reviews of Modern Physics, 38, 1-35, 1966.

Krankowsky, D., W. T. Kasprzak, and A. O. Nier, Mass spectrometric studies of the composition of the lower thermosphere during summer 1967, J. Geophys. Res., 73, No. 23, 7291-7306, 1968.

Mauersberger, K., D. Mueller, D. Offermann, and U. von Zahn, "A Mass Spectrometric Determination of the Neutral Constituents in the Lower Thermosphere above Sardinia," Journal of Geophysical Research, 73, 1071-1076, 1968.

Niemann, H. B. and J. R. Kreick, Application of a Quasi-Open Ion Source for Neutral Particle Density Measurements in the Thermosphere, University of Michigan Scientific Report 07065-3-S, August 1966.

Reber, C. A. and L. G. Hall, A Double-Focusing Magnetic Mass Spectrometer for Satellite Use, NASA Technical Note TN D-3211, Washington, D.C., March 1966.

Schultz, F. V., N. W. Spencer, and A. Reifman, Atmospheric Pressure and Temperature Measurements Between the Altitudes of 40 and 110 Kilometers, Upper Atmosphere Report No. 2, University of Michigan Research Institute, Ann Arbor, July 1948.

Simmons, R. W., M. F. Carter, and D. R. Taeusch, NASA 18.50 Thermosphere Probe Experiment, University of Michigan Sounding Rocket Flight Report 07065-8-R, May, 1968.

Spencer, N. W., L. H. Brace, G. R. Carignan, D. R. Taeusch, and H. B. Niemann, "Electron and Molecular Nitrogen Temperature and Density in the Thermosphere," Journal of Geophysical Research, 70, 2665-2698, 1965.

Spencer, N. W., G. P. Newton, G. R. Carignan, and D. R. Taeusch, Thermospheric temperature and density variations with increasing solar activity, Space Research X, 389-412, 1970.

von Zahn, U., Neutral air density and composition at 150 kilometers, J. Geophys. Res., 75, No. 28, 5517-5527, 1970.

Table I

Final Results of the Quadrupole Experiment

(Final results of the quadrupole experiment showing number densities, number density ratios, mass density of major constituents, mean molecular weight of major constituents, and kinetic temperature.)

| Alt [km] | $n_a(N_2)$ [$cm^{-3}$] | $n_a(0_2)$ [$cm^{-3}$] | $n_a(0)$ [$cm^{-3}$] | $\rho$ [$gr/cm^3$] | M | $n_a(0)/n_a(0_2)$ | $n_a(0)/n_a(N_2)$ | $n_a(0_2)/n_a(N_2)$ |
|---|---|---|---|---|---|---|---|---|
| 155 | $2.26 \times 10^{10}$ | $1.66 \times 10^{9}$ | | | | | | |
| 160 | 1.80 | $1.28 \times 10^{9}$ | | | | | | |
| 165 | 1.46 | $9.90 \times 10^{8}$ | | | | | | |
| 170 | $1.18 \times 10^{10}$ | 7.78 | $5.94 \times 10^{9}$ | $7.48 \times 10^{-10}$ | 24.31 | 7.60 | .504 | .066 |
| 175 | $9.68 \times 10^{9}$ | 6.22 | 5.18 | 6.21 | 24.07 | 8.49 | .548 | .064 |
| 180 | 7.95 | 4.95 | 4.72 | 5.21 | 23.87 | 9.49 | .591 | .062 |
| 185 | 6.60 | 3.98 | 4.22 | 4.40 | 23.63 | 10.63 | .637 | .060 |
| 190 | 5.50 | 3.22 | 3.80 | 3.74 | 23.39 | 11.83 | .693 | .059 |
| 195 | 4.53 | 2.62 | 3.41 | 3.15 | 23.13 | 13.02 | .753 | .058 |
| 200 | 3.83 | 2.14 | 3.08 | 2.71 | 22.91 | 14.39 | .804 | .056 |
| 205 | 3.22 | 1.74 | 2.78 | 2.33 | 22.73 | 15.92 | .858 | .054 |
| 210 | 2.71 | 1.43 | 2.50 | 2.00 | 22.50 | 17.41 | .915 | .053 |
| 215 | 2.29 | $1.18 \times 10^{8}$ | 2.25 | 1.72 | 22.27 | 19.07 | .974 | .051 |
| 220 | 1.94 | $9.69 \times 10^{7}$ | 2.03 | 1.49 | 22.16 | 20.95 | 1.041 | .050 |
| 225 | 1.64 | 8.04 | 1.83 | 1.29 | 21.89 | 22.90 | 1.116 | .049 |
| 230 | 1.39 | 6.64 | 1.67 | $1.13 \times 10^{-10}$ | 21.70 | 25.15 | 1.193 | .047 |
| 235 | $1.18 \times 10^{9}$ | 5.46 | 1.51 | $9.79 \times 10^{-11}$ | 21.47 | 27.91 | 1.280 | .046 |
| 240 | $9.93 \times 10^{8}$ | 4.53 | 1.37 | 8.50 | 21.26 | 30.46 | 1.380 | .045 |
| 245 | 8.42 | 3.75 | 1.26 | 7.46 | 21.03 | 33.33 | 1.478 | .044 |
| 250 | 7.11 | 3.11 | 1.14 | 6.50 | 20.84 | 36.33 | 1.580 | .043 |
| 255 | 6.06 | 2.59 | $1.03 \times 10^{9}$ | 5.69 | 20.62 | 39.77 | 1.691 | .043 |
| 260 | 5.14 | 2.15 | $9.43 \times 10^{8}$ | 5.01 | 20.41 | 43.77 | 1.824 | .042 |
| 265 | 4.38 | 1.79 | 8.58 | 4.41 | 20.20 | 48.04 | 1.955 | .041 |
| 270 | 3.72 | 1.49 | $7.81 \times 10^{8}$ | $3.88 \times 10^{-11}$ | 20.02 | 52.42 | 2.099 | .040 |
| 275 | 3.16 | $1.22 \times 10^{7}$ | | | | | | |
| 280 | $2.69 \times 10^{8}$ | | | | | | | |

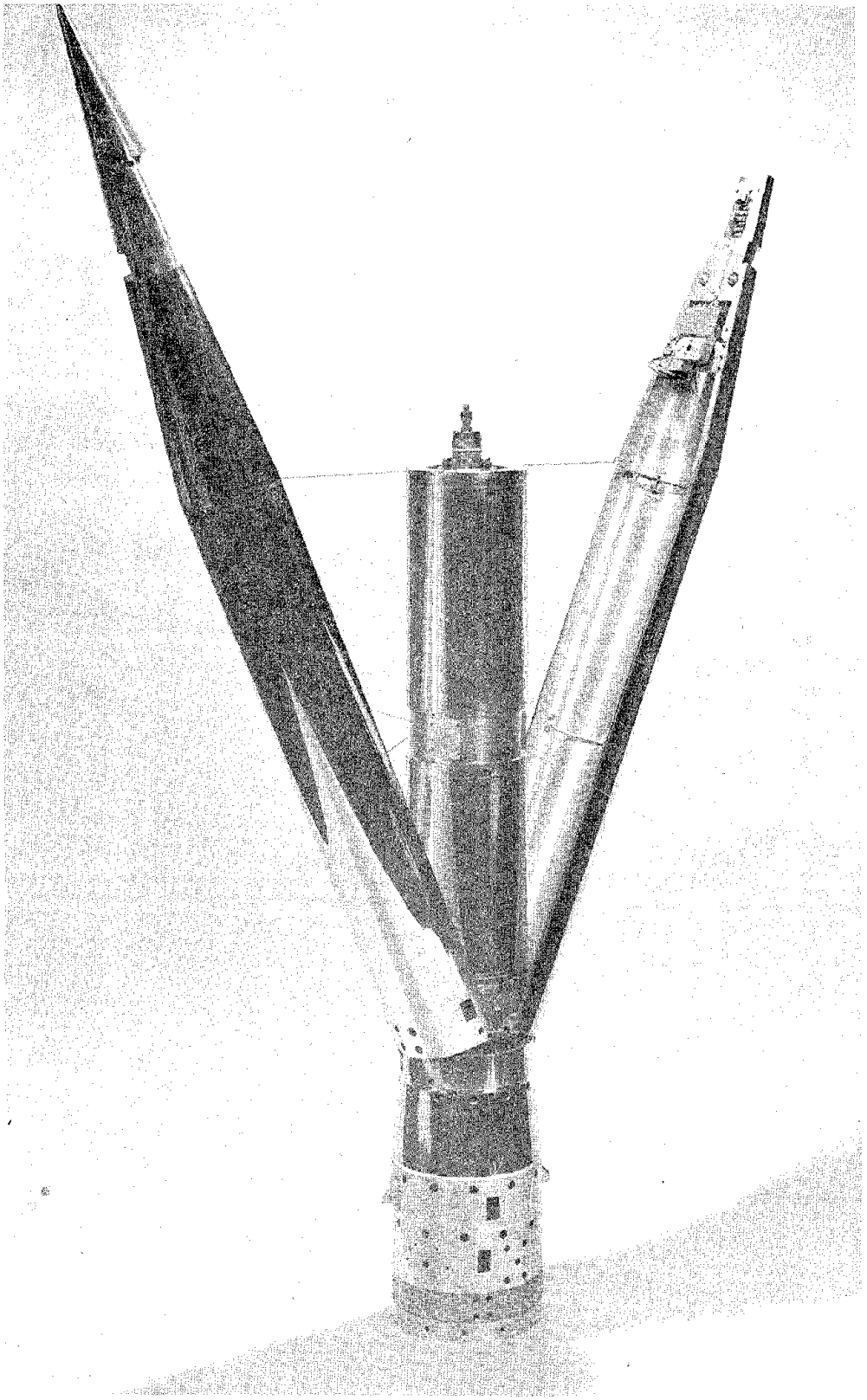

Figure 1. The Thermosphere Probe in the Clam Shell Nose Cone

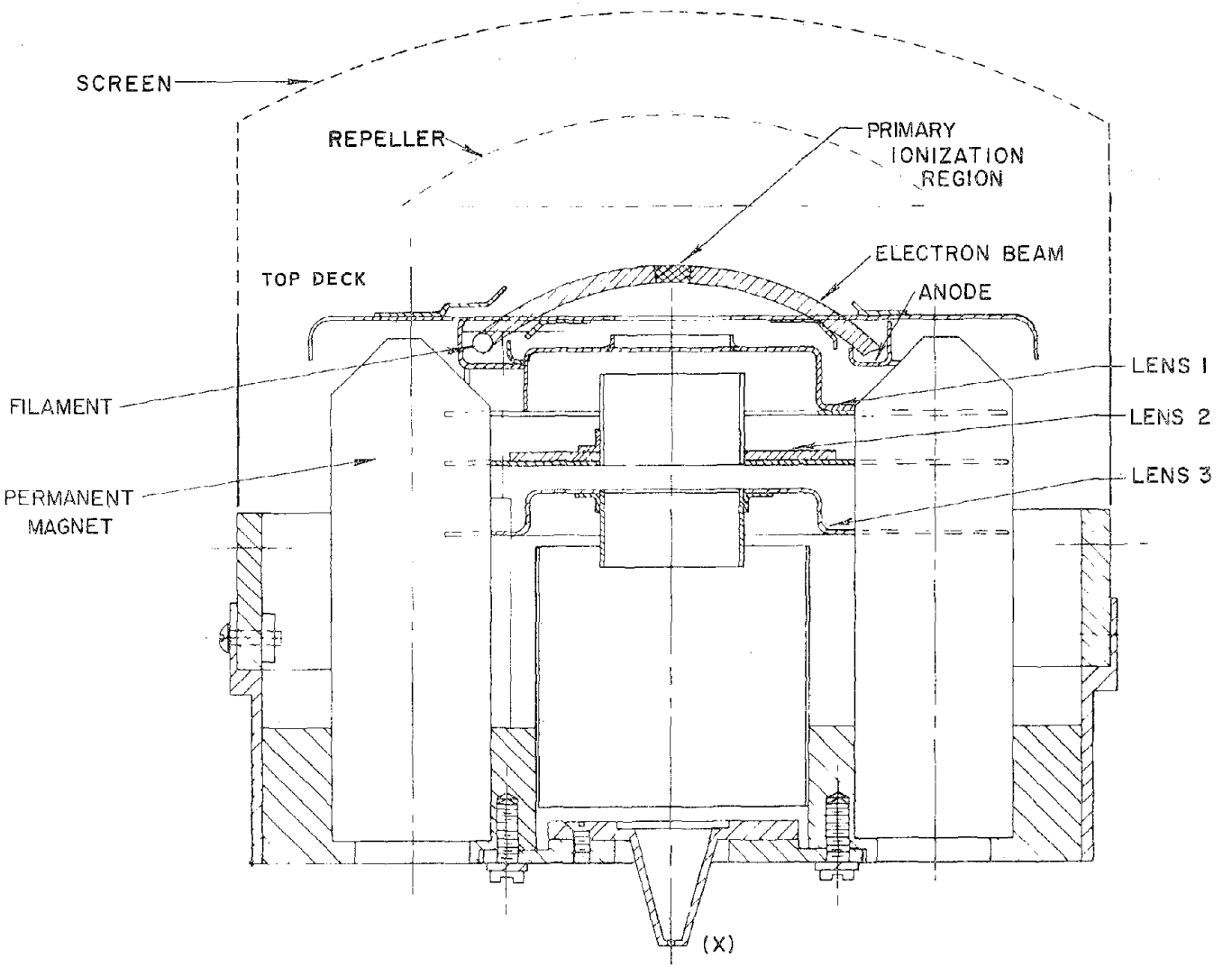


Figure 2. Cross Section of the Quadrupole Ion Source and Lens Chamber With the Electron Beam Trajectory

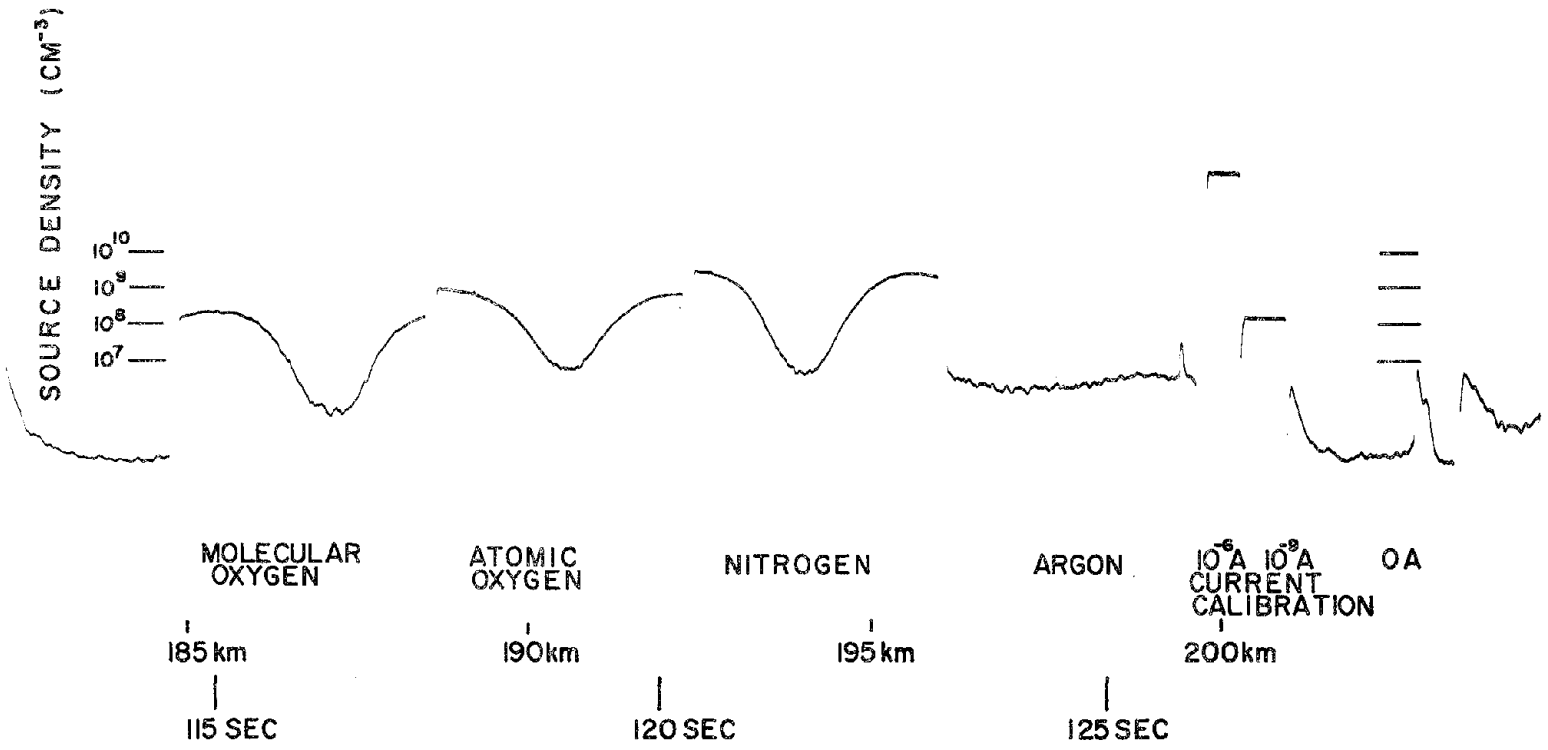


Figure 3. Sample of the Telemetry Record Obtained from the Quadrupole

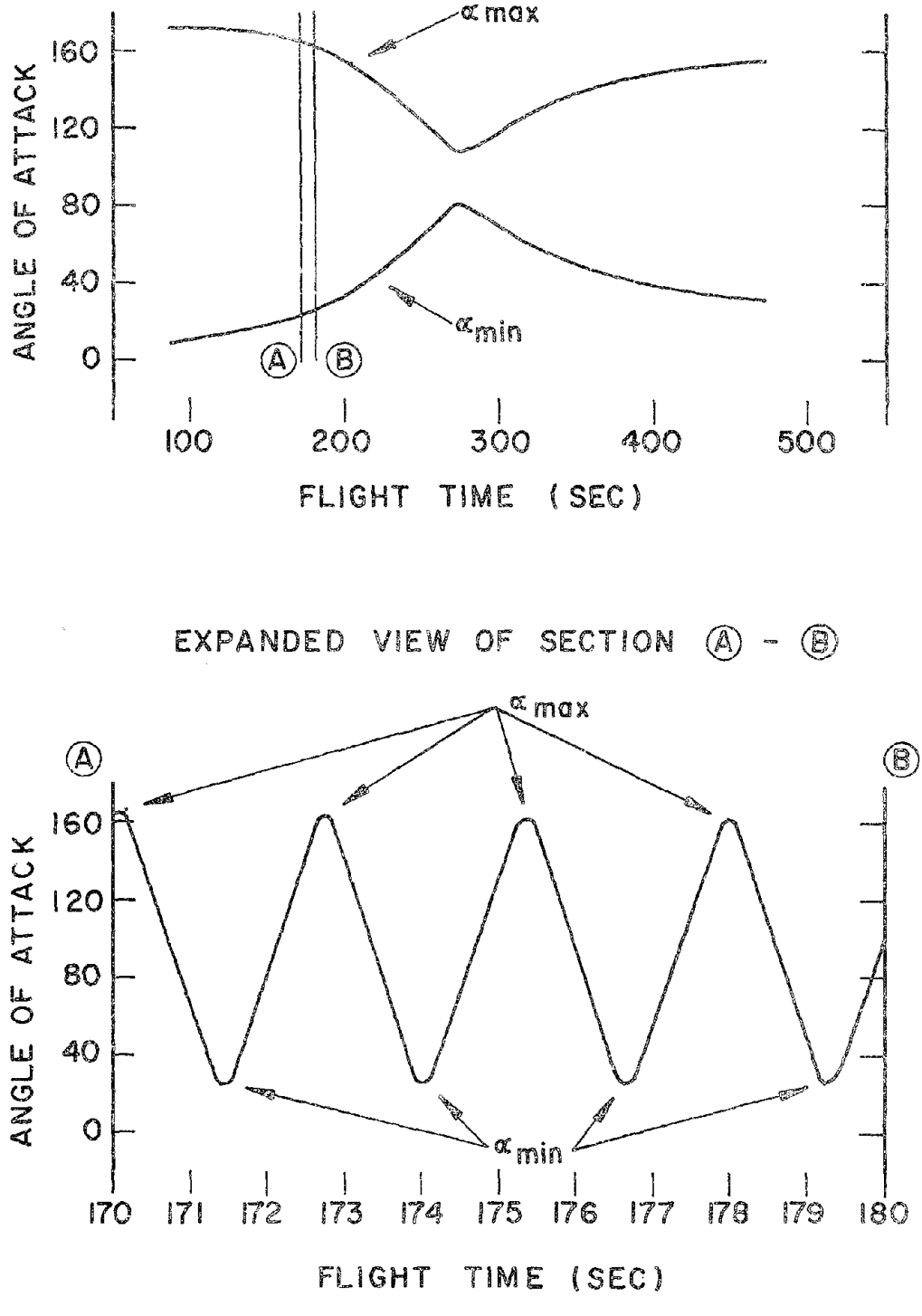


Figure 4. (a) Maximum and minimum angle of attack between the thermosphere probe axis and the velocity vector versus time from launch. (b) Expanded view of a section of Figure 4A.

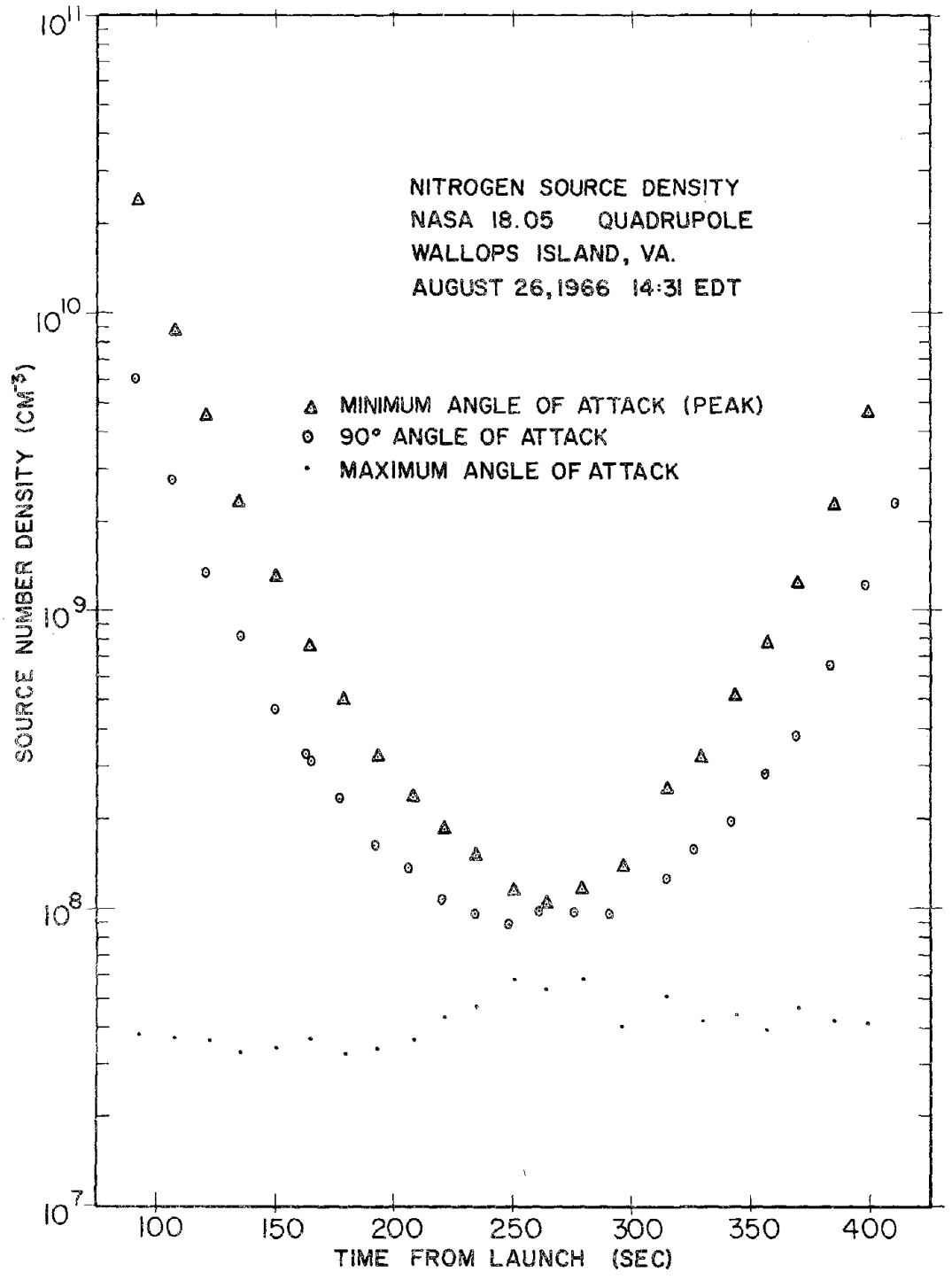


Figure 5. Ion source nitrogen density versus flight time for minimum angle of attack, 90 deg angle of attack, and maximum angle of attack.

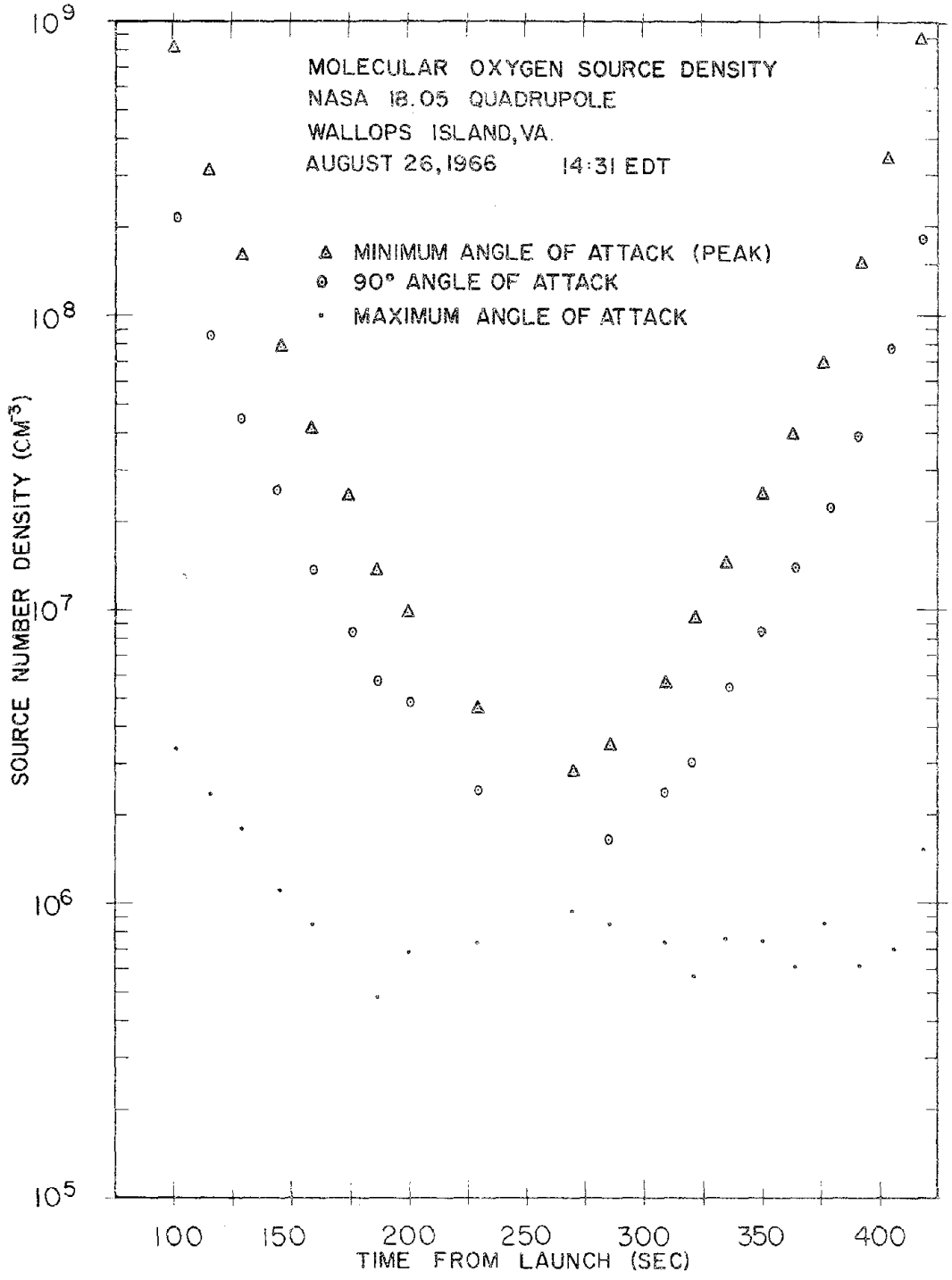


Figure 6. Ion source molecular oxygen density versus flight time for minimum angle of attack, 90 deg angle of attack, and maximum angle of attack.

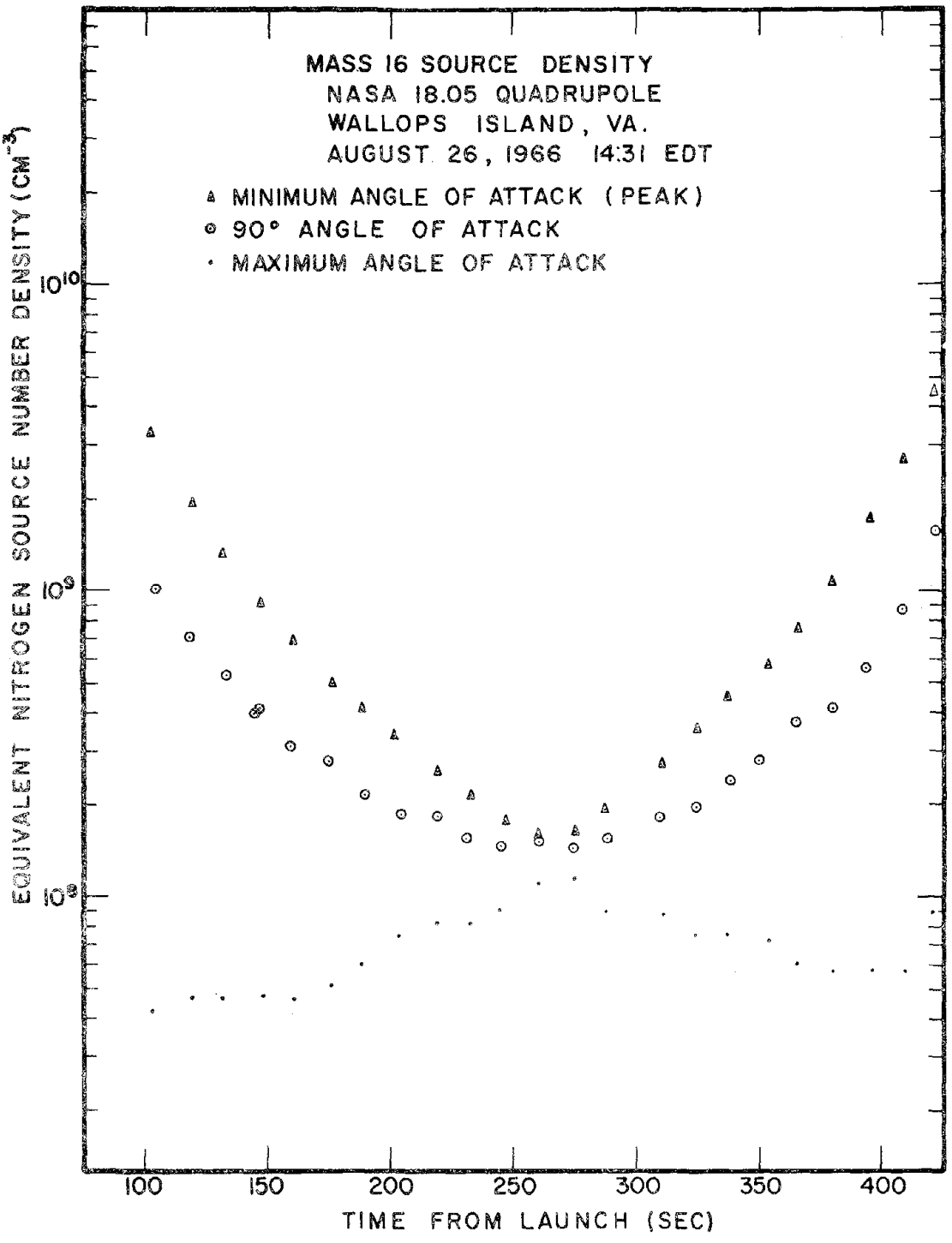


Figure 7. Ion source atomic oxygen density versus flight time for minimum angle of attack, 90 deg angle of attack, and maximum angle of attack.

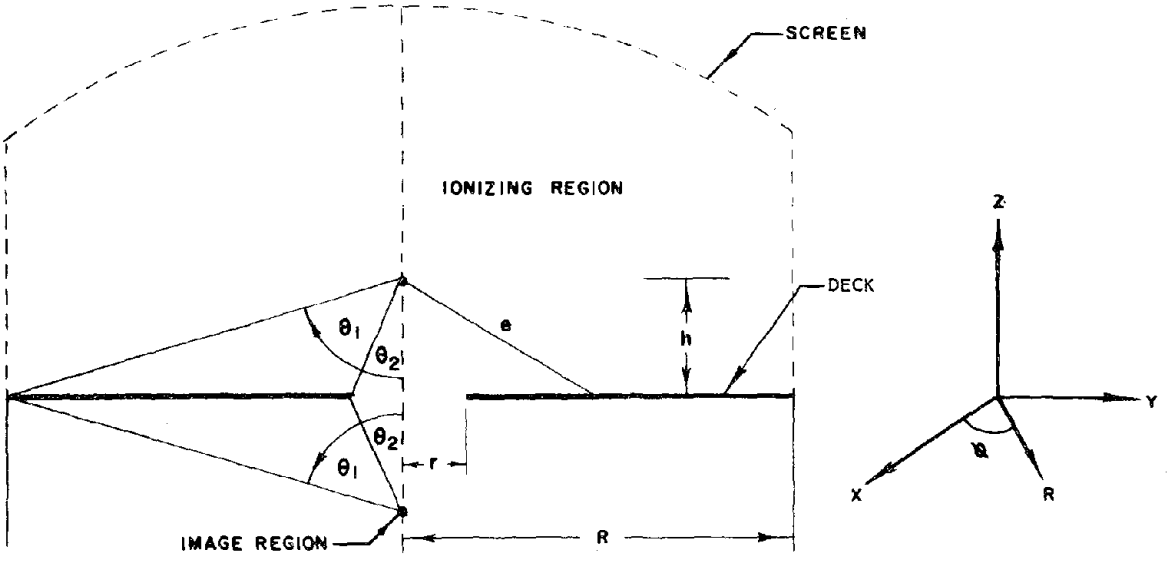


Figure 8. Simplified Model of the Geometry of the Quadrupole Ion Source

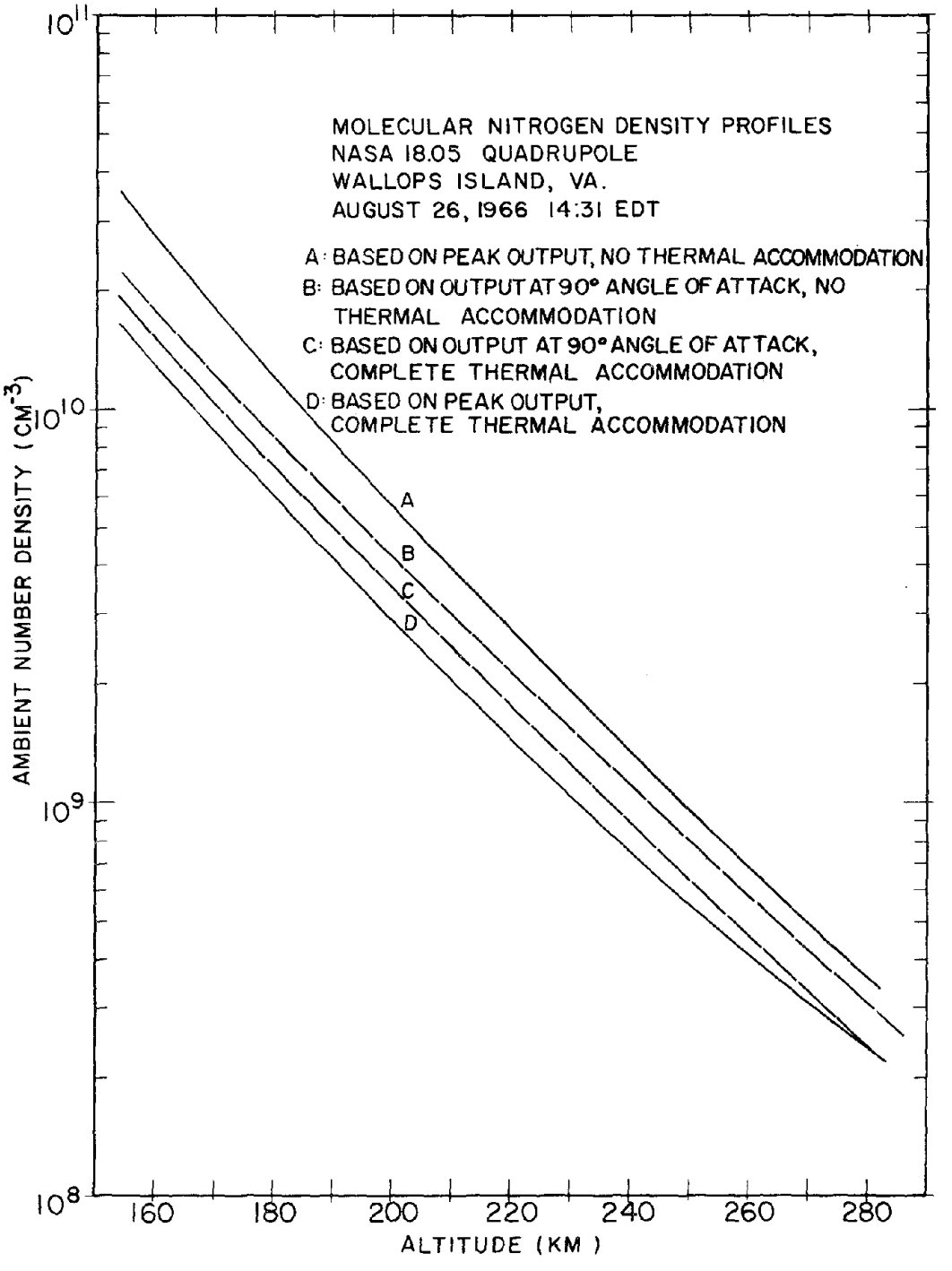


Figure 9. Computed molecular nitrogen density versus altitude for minimum angle of attack and 90 deg angle of attack assuming no thermal accommodation (curves A and B), and complete thermal accommodation (curves C and D).

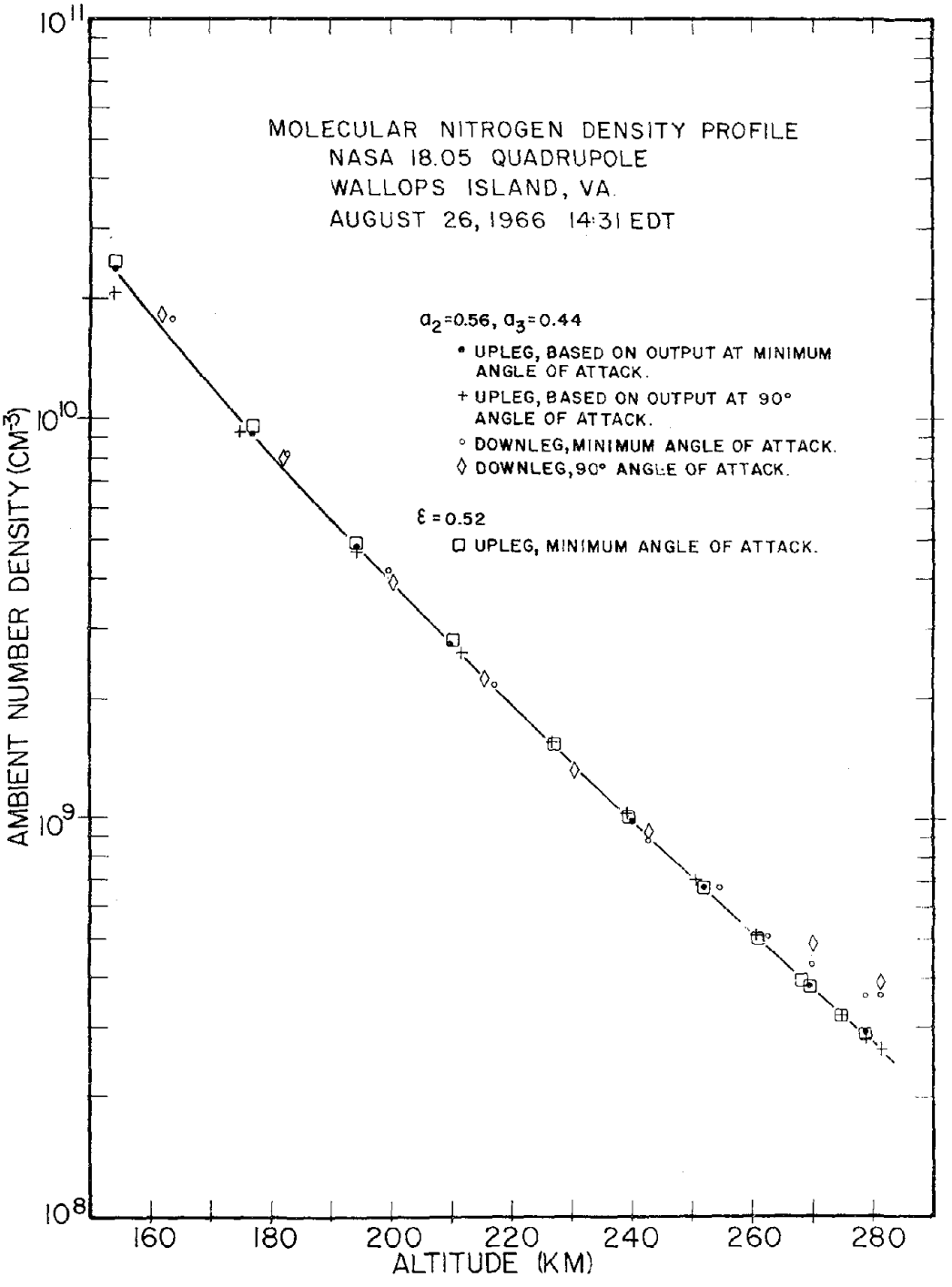


Figure 10. Ambient molecular nitrogen density versus altitude obtained from the curves of Figure 9 by varying the coefficients $a_2$ and $a_3$ or $\epsilon$. The dashed line shows the nitrogen density profile obtained from the omegatron.

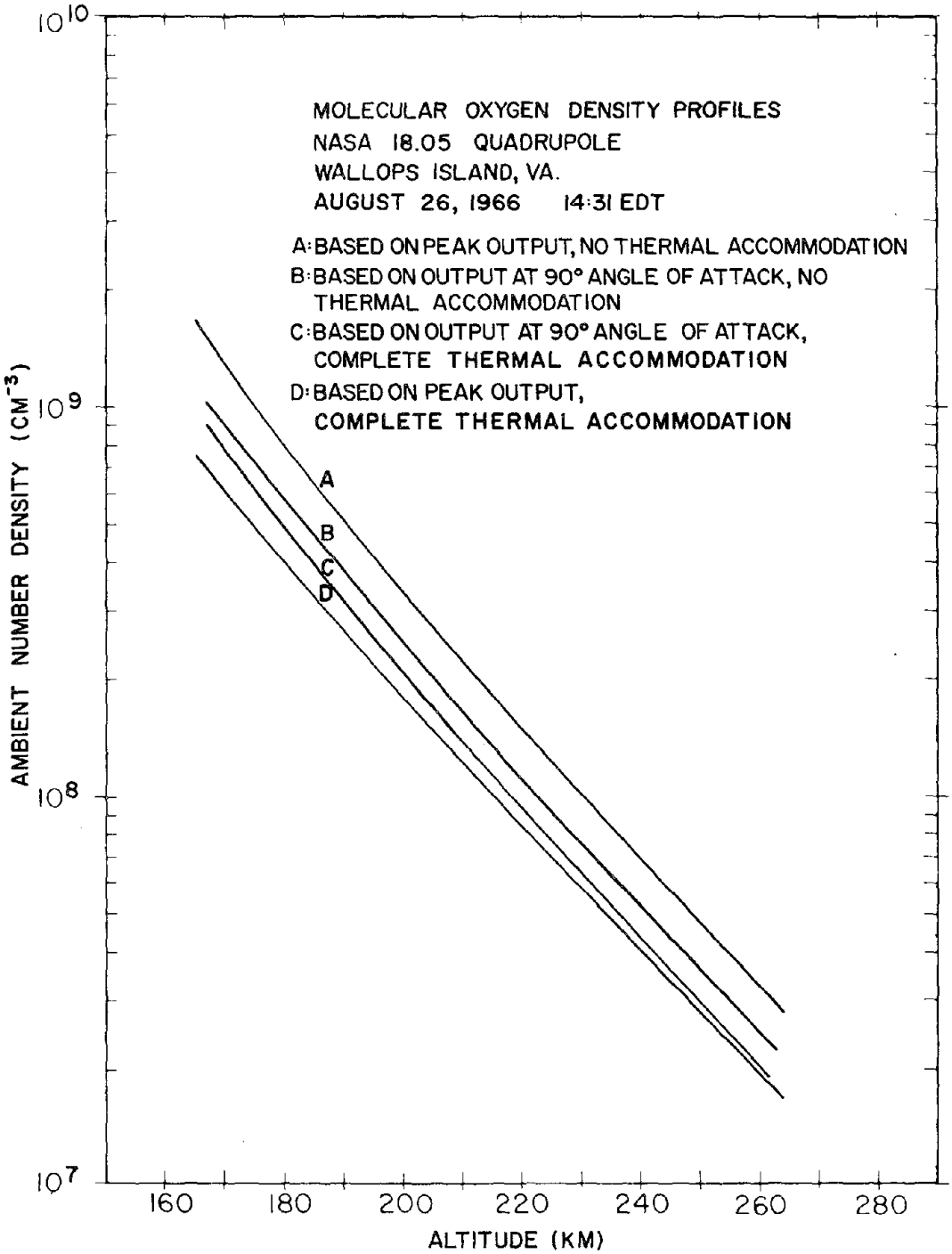


Figure 11. Computed molecular oxygen density versus altitude for minimum angle of attack and 90 deg angle of attack assuming no thermal accommodation (curves A and B), and complete thermal accommodation (curves C and D).

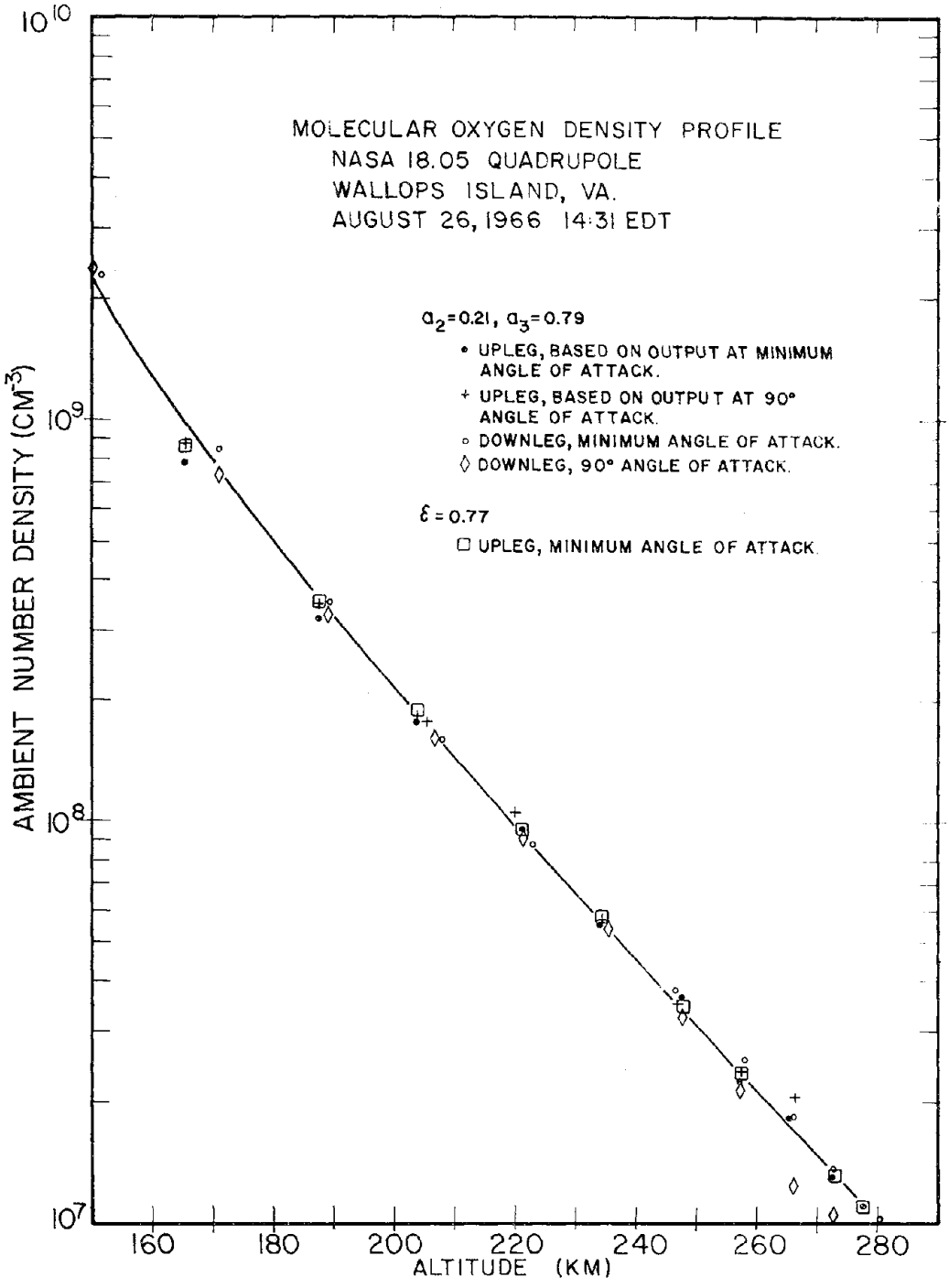


Figure 12. Ambient molecular oxygen density versus altitude, obtained from the curves of Figure 11 by varying the coefficients $a_2$ and $a_3$ or $\epsilon$.

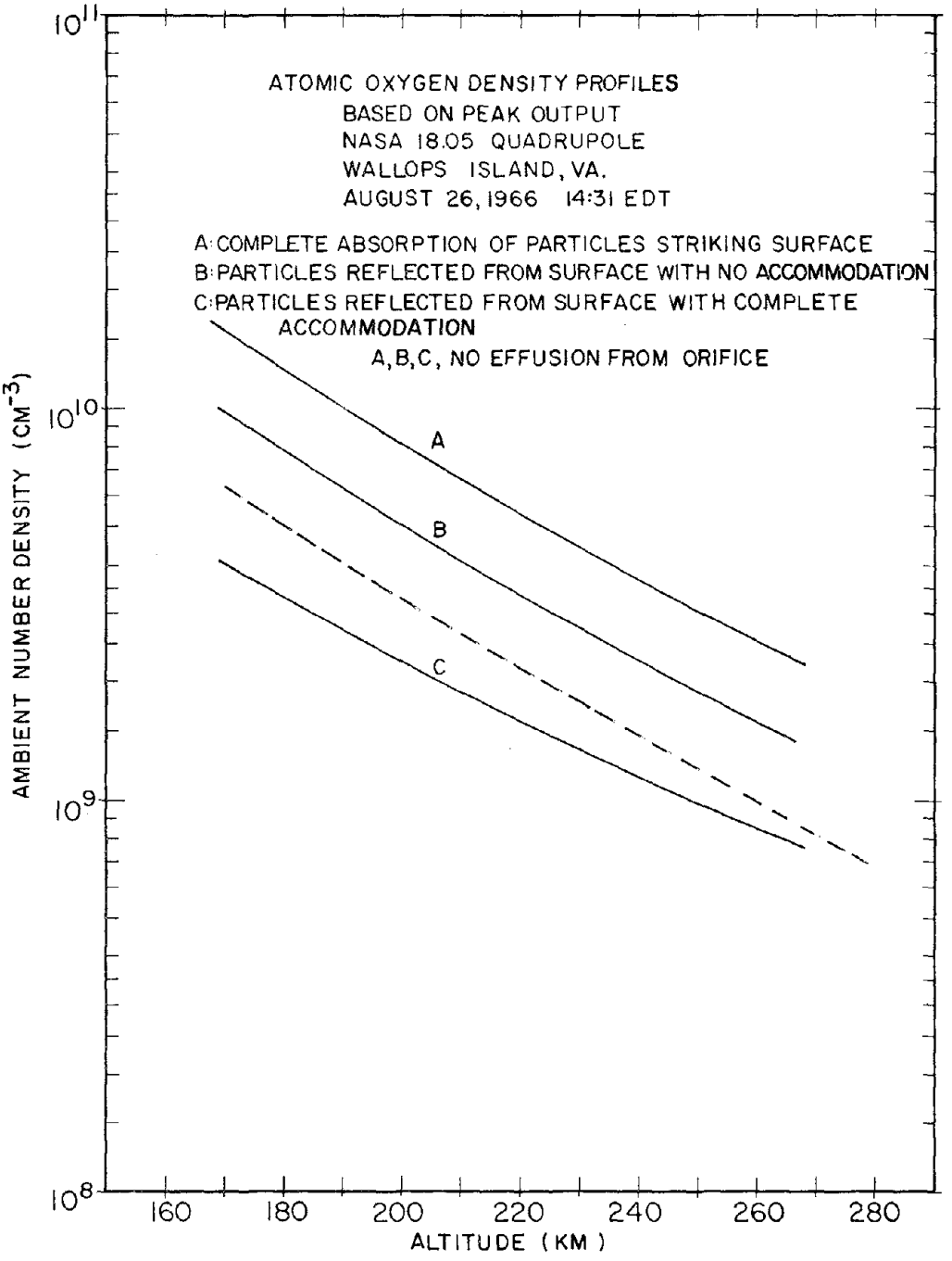


Figure 13. Computed atomic oxygen density versus altitude for minimum angle of attack assuming (1) complete adsorption of particles striking the surface (curve A), (2) no adsorption and no thermal accommodation of particles striking the top deck (curve B), (3) no adsorption and complete thermal accommodation of particles striking the top deck (curve C). A theoretical profile computed by assuming diffusive and thermal equilibrium and by using the omegatron temperature is shown by the dashed line.

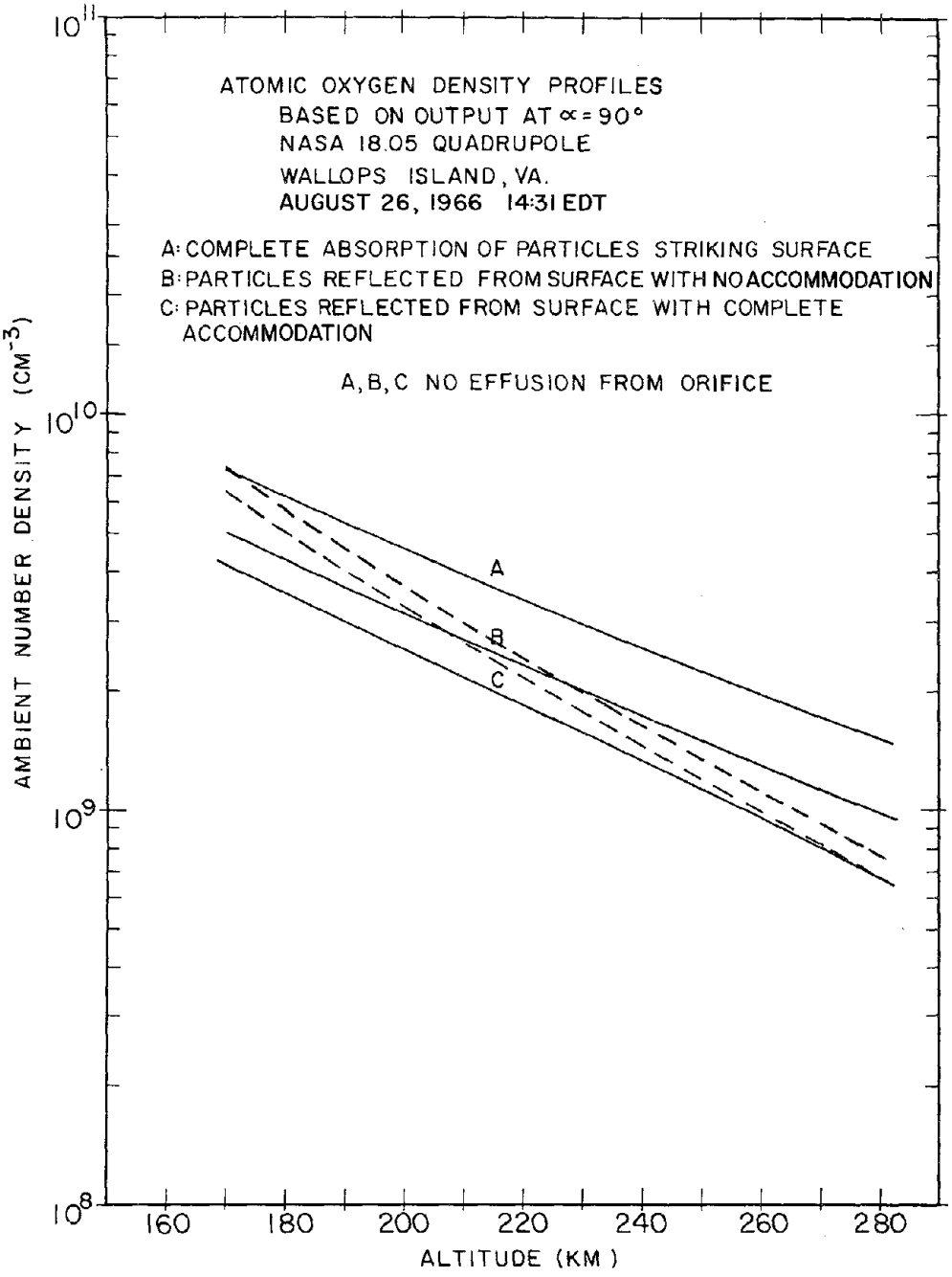


Figure 14. Computed atomic oxygen density versus altitude for 90 deg angle of attack assuming (1) complete adsorption of particles striking the surface (curve A), (2) no adsorption and no thermal accommodation of particles striking the top deck (curve B), (3) no adsorption and no thermal accommodation of particles striking the top deck (curve C). The two dashed lines each result from assuming diffusive and thermal equilibrium and from using the omegatron temperature. The top dashed line assumes complete adsorption at 170 km. The bottom dashed line assumes complete accommodation and no adsorption at high altitudes.

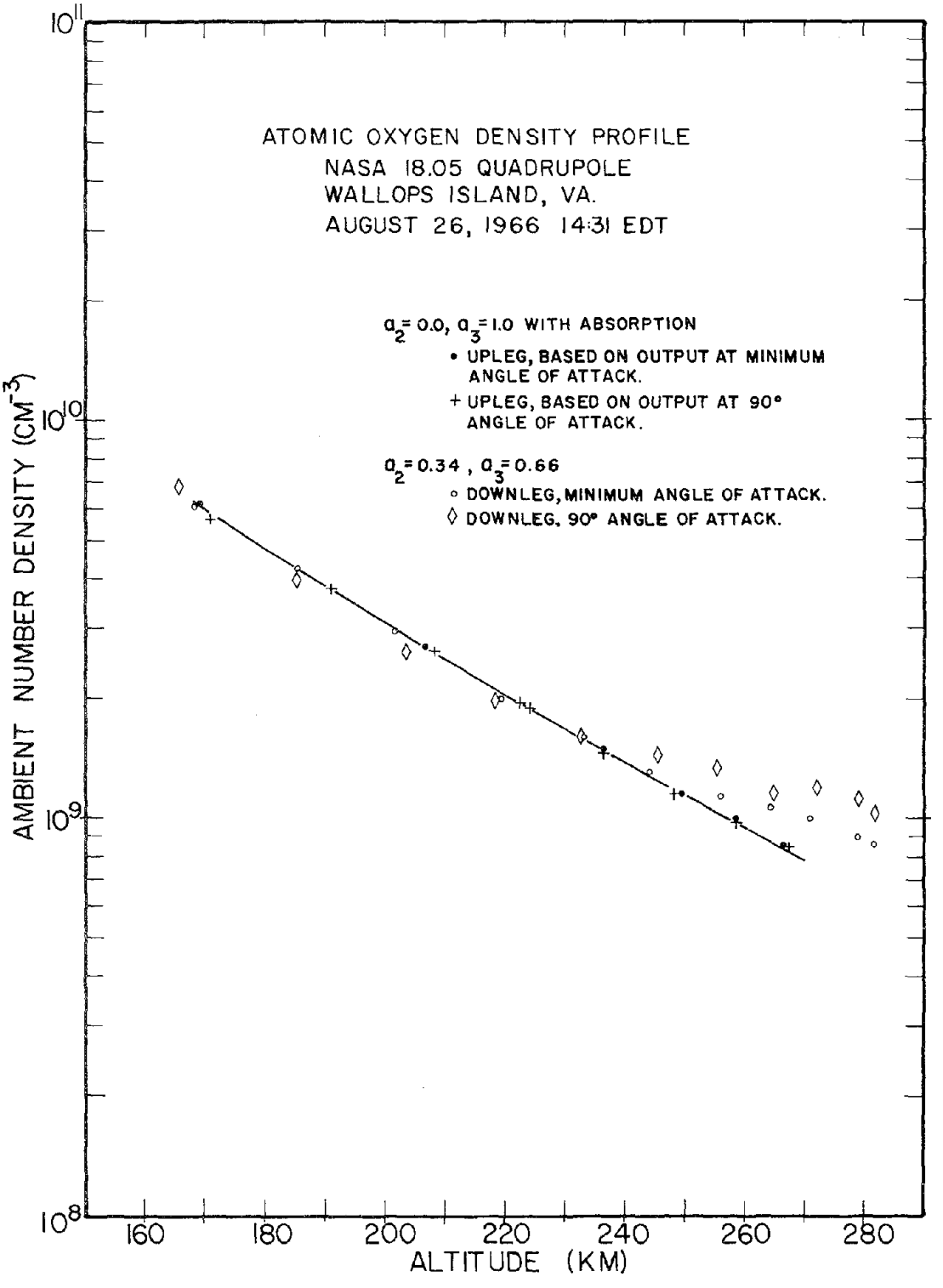


Figure 15. Ambient Atomic Oxygen Density Versus Altitude

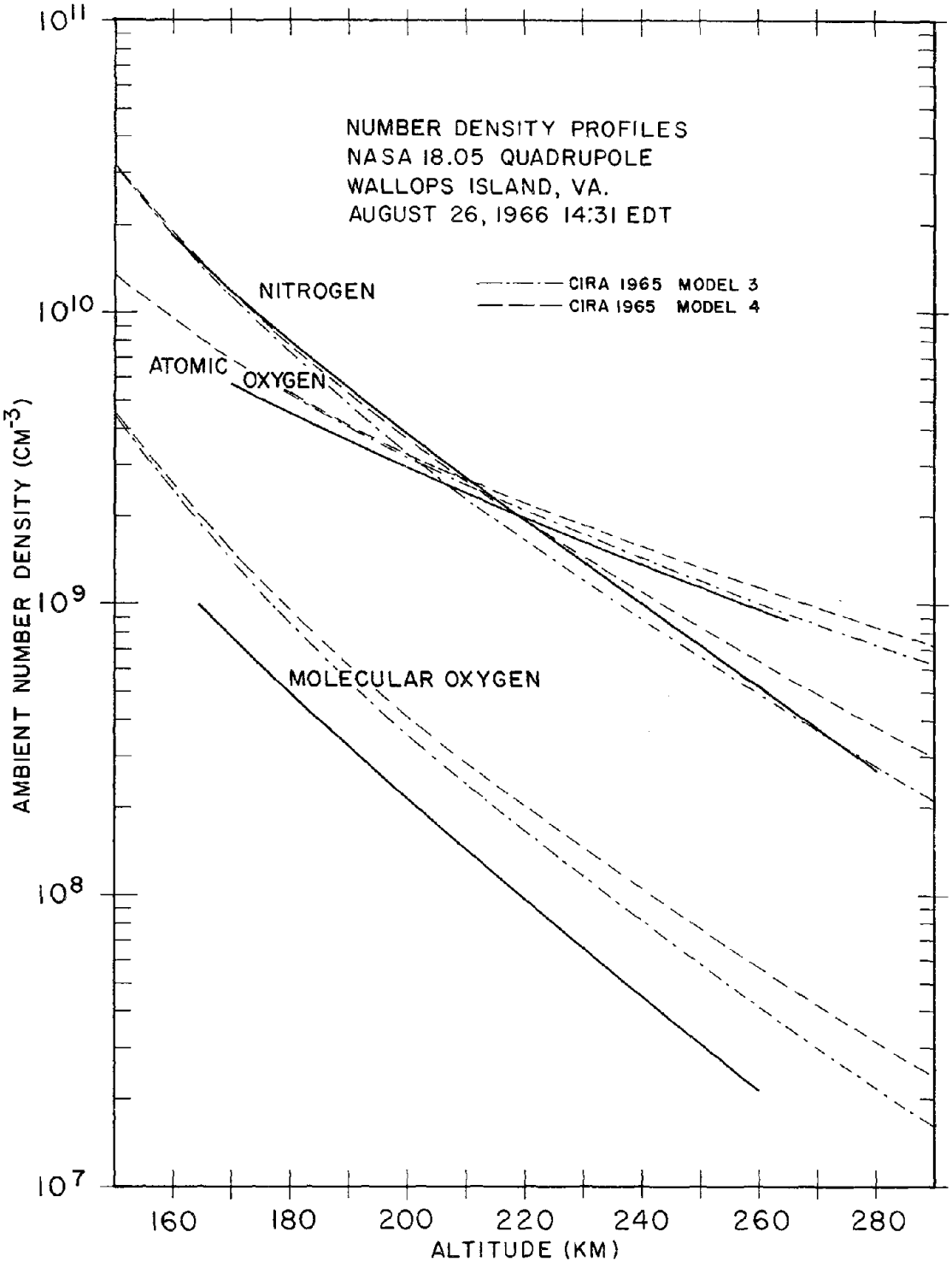


Figure 16. Ambient particle densities of molecular nitrogen, atomic and molecular oxygen versus altitude.

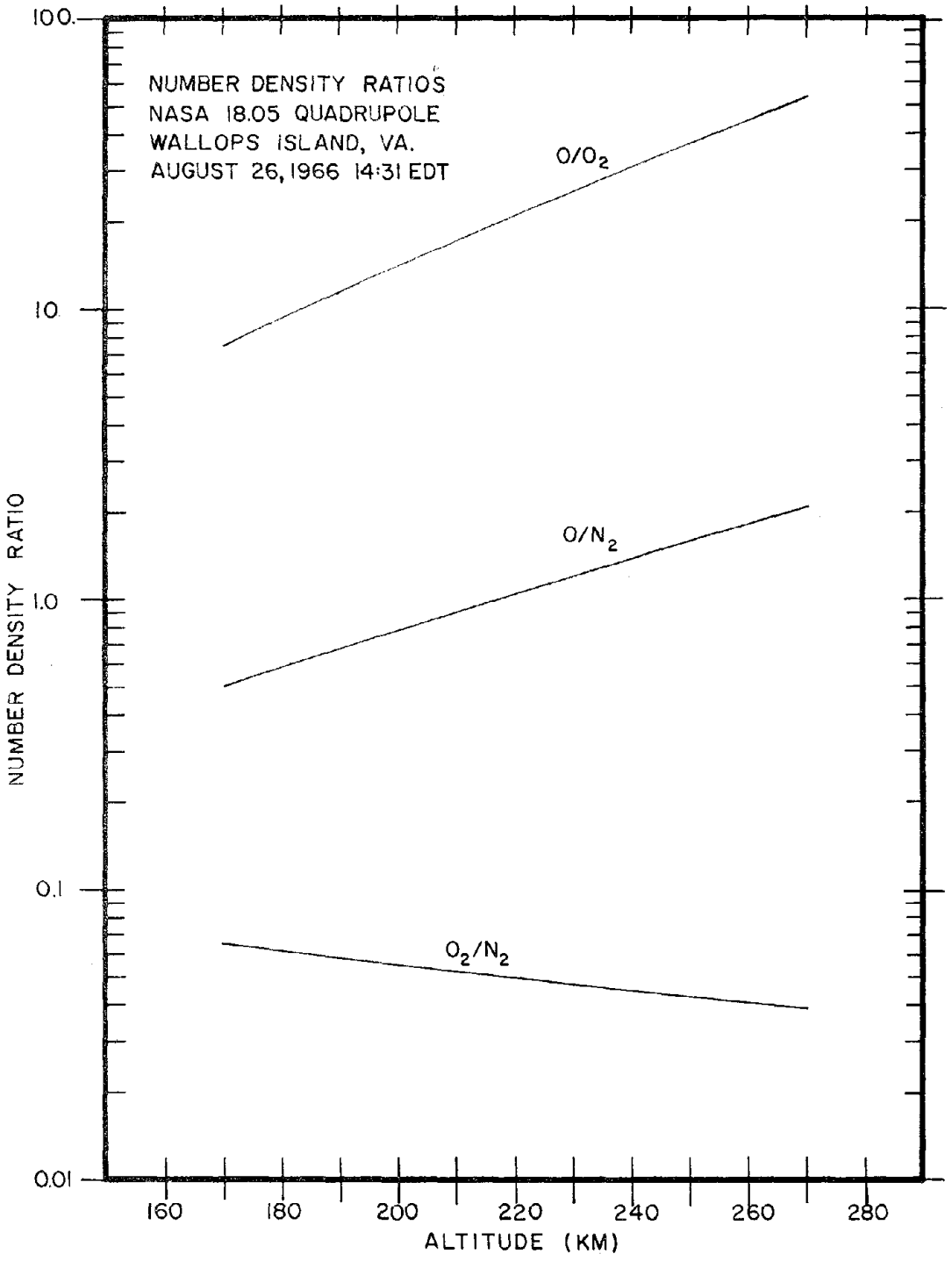


Figure 17. Ambient particle density ratios of atomic to molecular oxygen, atomic oxygen to molecular nitrogen, and of molecular oxygen to molecular nitrogen versus altitude.

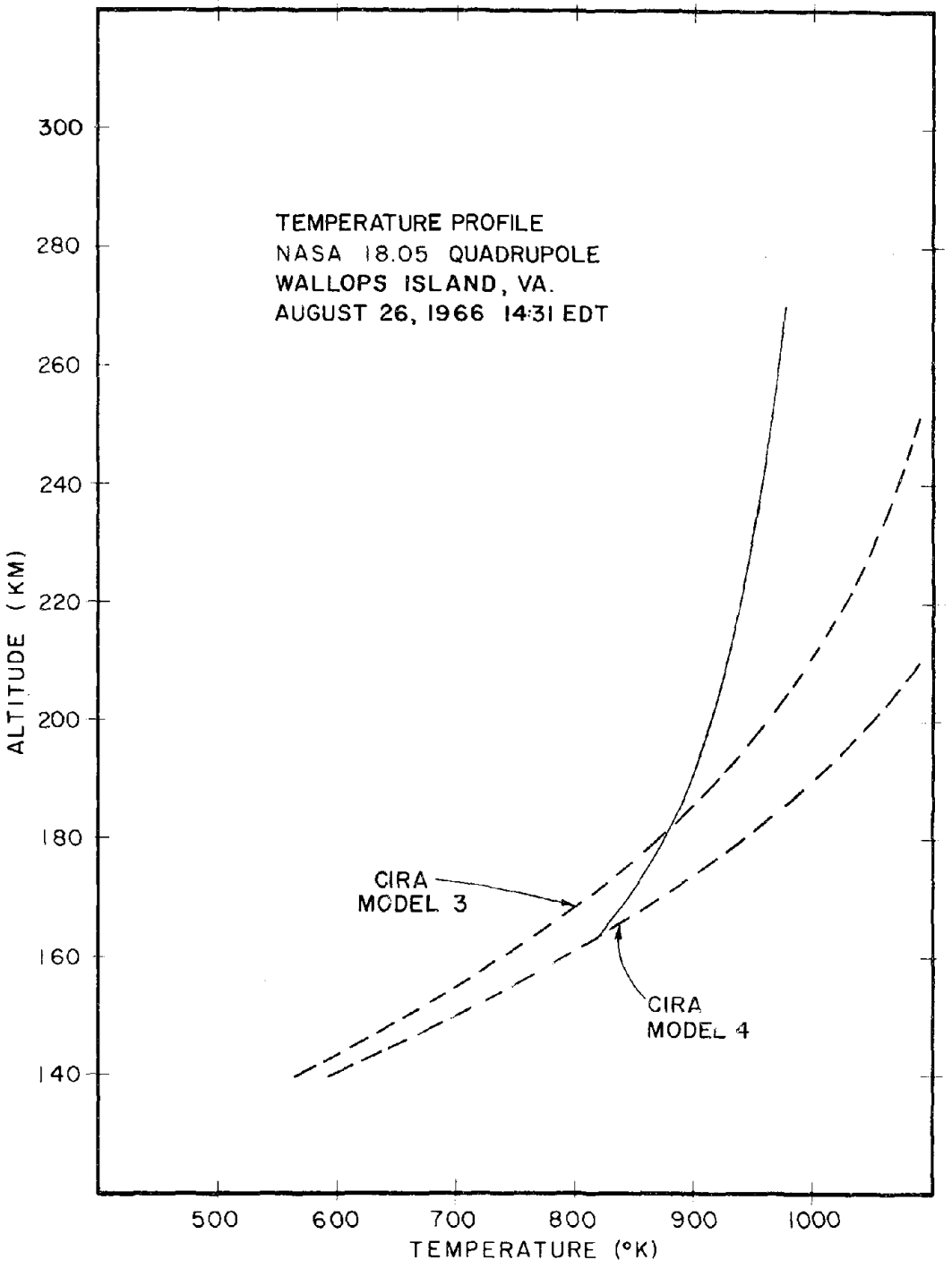


Figure 18. Ambient temperature versus altitude. The dashed lines show the value of the CIRA 1965 models 3 and 4 for 1400 hours.

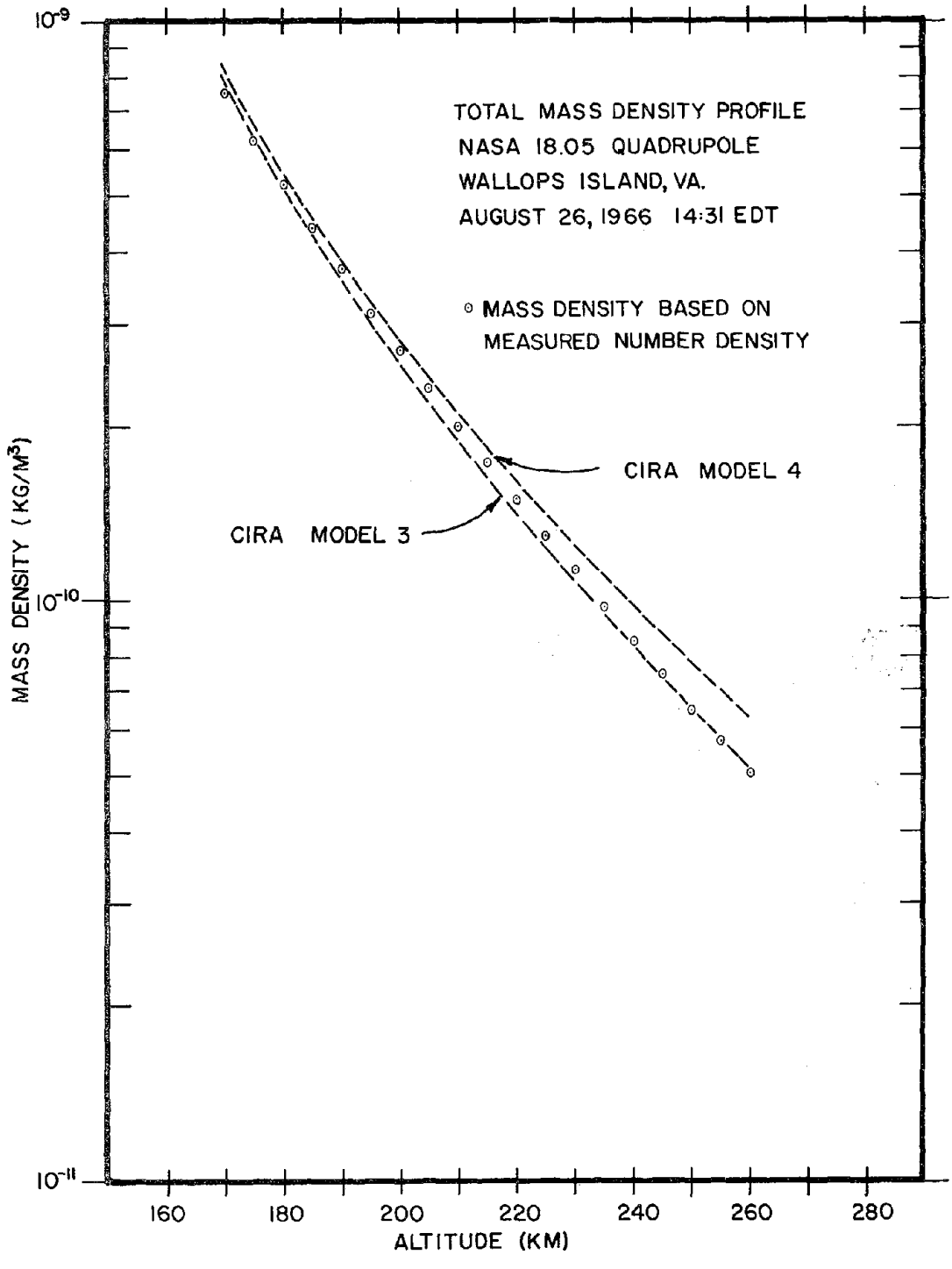


Figure 19. Total mass density of major constituents versus altitude. The dashed lines show the value of the CIRA 1965 models 3 and 4 for 1400 hours.

## APPENDIX A

## A SIMPLE MODEL FOR THERMAL ACCOMMODATION OF NEUTRAL PARTICLES ON THE SURFACE OF THE ION SOURCE

The derivation of the thermal accommodation equation is based on the assumption that all particles which collide with the top surface of the ion source lose an amount of energy which is proportional to the initial energy with which they strike the surface.

Defining an accommodation efficiency as

$$\epsilon = \frac{|\vec{u}-\vec{v}|^2 - |\vec{v}'|^2}{|\vec{u}-\vec{v}|^2 - |\vec{v}|^2 \dfrac{C_0^2}{C_s^2}}, \tag{A.1}$$

where

$\vec{u}$ = probe velocity,

$\vec{u}-\vec{v}$ = initial velocity before the collision,

$\vec{v}'$ = final velocity after the collision,

$C_0 = \sqrt{2kT_0/m}$, most probable speed in a gas at ambient temperature,

$C_s = \sqrt{2kT_s/m}$, most probable speed in a gas at the temperature of the surface,

where

$k$ = Boltzmann's constant, $1.38 \times 10^{-23}$ J/°K,

$T_0$ = ambient neutral particle temperature,

$T_s$ = surface temperature,

$m$ = molecular weight of the specie measured.

From Equation (A.1), we obtain the final velocity ratio

$$\frac{|\vec{v}'|^2}{C_0^2} = (1 - \epsilon) \frac{|\vec{u}-\vec{v}|^2}{C_0^2} + \epsilon \frac{|\vec{u}|^2}{C_s^2} . \tag{A.2}$$

The Maxwell-Boltzmann velocity distribution which describes the ambient gas in a moving coordinate system is

$$f(\vec{u},\vec{v}) = \frac{1}{C_0^3 \pi^{3/2}} \exp - \left[\frac{|\vec{u}-\vec{v}|^2}{C_0^2}\right] . \tag{A.3}$$

With the assumption made above, the term $|\vec{u}-\vec{v}|^2/C_0^2$ in the exponent of Equation (A.3) is replaced by Equation (A.2) and the distribution function of the outgoing gas can be written

$$f'(\vec{u},\vec{v}) = K \exp - \left[\frac{v'}{C_0}\right]^2 = K \exp - \left[(1 - \epsilon) \frac{|\vec{u}-\vec{v}|^2}{C_0^2} + \epsilon \frac{|\vec{v}|^2}{C_s^2}\right],$$

where K is a constant to be determined from the condition

$$\int f'(\vec{u},\vec{v})\, d^3v = 1 .$$

(all velocity space)

This condition yields

$$K = \frac{1}{C_0^{3/2} \pi^{3/2}} \left[1 + \left(\frac{T_0}{T_s} - 1\right) \epsilon\right]^{3/2} ,$$

and, therefore, the velocity distribution of the outflowing gas is

$$S_z' = \sqrt{\frac{1-\epsilon}{1+\frac{\epsilon}{1-\epsilon}\frac{T_0}{T_s}}}\, S_z \text{ and } S_{i_z}' = \sqrt{\frac{\epsilon}{1-\epsilon}\frac{T_0}{T_s}}\, S_z .$$

Equating $\Gamma_1$ to $\Gamma_2$, we have

$$\frac{n_0 \bar{C}_0}{4} f(S_z) = \frac{n_s \bar{C}_0}{4} H(\epsilon, S_z)$$

and, solving for $n_s$,

$$n_s = n_0 \frac{f(S_z)}{H(\epsilon, S_z)} . \tag{A.8}$$

The density in the ionizing region is now obtained by dividing the outgoing differential flux by the particle velocity, by integrating over all possible velocities, and then by multiplying by the solid angle subtended by the surfaces. If $n_d$ is the particle density in the ionization region,

$$n_d = \frac{\Omega_s}{2\pi}\int \frac{d\Gamma_2}{v_z} = \frac{\Omega_s}{2\pi} n_s \int_0^\infty \int_{-\infty}^\infty \int_{-\infty}^\infty f'(\vec{u},\vec{v})\, dv_x\, dv_y\, dv_z \tag{A.9}$$

where $\Omega_s$ is the solid angle subtended by the surface,

$$\Omega_s = 2\pi(\cos\theta_2 - \cos\theta_1) .$$

Thus, after integration,

$$n_d = \frac{(\cos\theta_2 - \cos\theta_1)}{2} n_s \left[1 + \text{erf}(S_z')\right] \exp\left(-S_{i_z}^2\right) \tag{A.10}$$

and by substituting Equations (A.7) and (A.8) into (A.10),

$$n_d = n_0 \frac{f(S_z)}{f(S_z')} \left[1 + \text{erf}(S_z')\right] \sqrt{1 + \epsilon\left(\frac{T_0}{T_s}\right) - 1}\, \frac{(\cos\theta_2 - \cos\theta_1)}{2} . \tag{A.11}$$

$$f'(\vec{u},\vec{v}) = \frac{\left(1 + \frac{T_0}{T_s} - 1\ \epsilon\right)^{3/2}}{C_0^3\ \pi^{3/2}} \exp - \ (1-\epsilon)\ \frac{|\vec{u}-\vec{v}|^2}{C_0^2} + \epsilon\ \frac{|\vec{v}|^2}{C_s^2} \ . \qquad (A.4)$$

Proceeding as in Niemann and Kreick (1966) by computing and equating the incoming and outgoing flux we find the surface particle density.

The incoming flux is given as

$$\Gamma_1 = n_0 \int_0^\infty \int_{-\infty}^\infty \int_{-\infty}^\infty v_z\ f(\vec{u},\vec{v})\ dv_x\ dv_y\ dv_z = \frac{n_0 \bar{C}_0}{4}\ f(S_z)\ , \qquad (A.5)$$

where

$n_0$ = ambient particle density,

$\bar{C}_0$ = average thermal velocity, $\bar{C}_0 = \sqrt{8kT_0/\pi m}$ ,

$f(S) = \exp(-S^2) + \sqrt{\pi}\ S[1 + \mathrm{erf}(S)]$ ,

$S_z = u_z/C_0$, the ratio of the z-component of the vehicle velocity to the most probable thermal velocity.

Similarly, the outgoing flux is

$$\Gamma_2 = n_s \int_0^\infty \int_{-\infty}^\infty \int_{-\infty}^\infty v_z\ f'(\vec{u},\vec{v})\ dv_x\ dv_y\ dv_z = \frac{n_s \bar{C}_0}{4}\ H(\epsilon, S_z)\ , \qquad (A.6)$$

where $n_s$ is the surface gas density and

$$H(\epsilon, S_z) = \frac{\exp\left(-S_{i_z}'\right)^2}{1 + \left(\frac{T_0}{T_s} - 1\right)\ \epsilon}\ f(S_z')\ , \qquad (A.7)$$

with

## APPENDIX B

## THE ATOMIC OXYGEN-SURFACE INTERACTION MODEL

Atomic oxygen was partially adsorbed on the deck of the quadrupole. The general features of this adsorption were investigated by using the simple model derived below. This model assumes that (1) the time required to achieve steady state is short compared to the tumble period, (2) the model parameters are functions of the quadrupole angle of attack, that is, functions of the angular distribution of the incoming flux, and (3) the second and all higher adsorbed gas layers are quite similar to each other but different from the first layer.

Let

$b_1$ = evaporation rate from the first layer,

$b$ = evaporation rate from the second and higher order layers,

$a_1$ = sticking probability on unoccupied sites,

$a$ = sticking probability on occupied sites,

$\gamma_1$ = recombination coefficient of atomic oxygen for the first layer

$\gamma$ = recombination coefficient of atomic oxygen for the second and higher order layers,

$c_1$ = rate of diffusion of atomic oxygen into the solid,

$\Gamma_1$ = incoming atomic oxygen flux,

$\Gamma_2$ = outgoing atomic oxygen flux,

$S_i$ = fractional surface coverage of the $i^{th}$ surface containing i layers of atomic oxygen, $i = 0, 1, \ldots$

Assuming steady state surface conditions, we obtain from the conservation of fractional coverage for the first layer,

$$S_1 b_1 + \Gamma_1 \gamma_1 S_1 + c_1(1 - S_0) = \Gamma_1 a_1 S_0 . \quad (B.1)$$

Similarly for the second layer,

$$\Gamma_1 a_1 S_0 + S_2 b + \Gamma_1 \gamma S_2 = S_1 b_1 + \Gamma_1 \gamma_1 S_1 + c_1(1 - S_0) + \Gamma_1 a S_1 . \quad (B.2)$$

From Equations (B.1) and (B.2),

$$S_2 b + \Gamma_1 \gamma S_2 - \Gamma_1 a S_1 = 0 . \quad (B.3)$$

Thus, in general we can write for the second and higher order layers

$$S_i b + \Gamma_1 \gamma S_i - \Gamma_1 a S_{i-1} = 0, \quad i = 2, 3, \ldots . \quad (B.4)$$

Solving Equation (B.1) for $S_1$,

$$S_1 = \frac{a_1 \Gamma_1 + c_1}{\gamma_1 \Gamma_1 + b_1} S_0 - \frac{c_1}{\gamma_1 \Gamma_1 + b_1} = Y S_0 - Z , \quad (B.5)$$

where

$$Y \equiv \frac{a_1 \Gamma_1 + c_1}{\gamma_1 \Gamma_1 + b_1}$$

and

$$Z \equiv \frac{c_1}{\gamma_1 \Gamma_1 + b_1} ,$$

and solving Equation (B.4) for $S_i$ we have

$$S_i = \frac{a \Gamma_1}{\gamma \Gamma_1 + b} S_{i-1} \equiv X S_{i-1}, \quad i \geq 2 , \quad (B.6)$$

where

$$X \equiv \frac{a\Gamma_1}{\gamma\Gamma_1 + b} ,$$

From the definition of $S_i$ we have the condition

$$\sum_{i=0}^{\infty} S_i = 1, \tag{B.7}$$

or with Equations (B.5) and (B.6)

$$S_0 + S_1 + S_2 + \ldots$$

$$= S_0 + (YS_0 - Z) + (YS_0 - Z)\,X + (YS_0 - Z)\,X^2 + \ldots$$

$$= S_0 + (YS_0 - Z) \sum_{i=0}^{\infty} X^i = 1 . \tag{B.8}$$

If $X < 1$, then the series converges and

$$S_0 = \frac{1 - X + Z}{1 - X + Y} . \tag{B.9}$$

The above equation is valid if the surface properties of atomic oxygen are invariant from layer to layer. Now,

$$\Gamma_2 = \Gamma_1 - \Gamma_1 S_1 \gamma_1 - \Gamma_1 \gamma \left\{\sum_{i=2}^{\infty} S_i\right\} - c_1(1 - S_0) ,$$

and if the fractional adsorption is defined

$$F \equiv \frac{\Gamma_1 - \Gamma_2}{\Gamma_1} = \gamma_1 S_1 + \gamma(1 - S_0 - S_1) + \frac{c_1}{\Gamma_1}(1 - S_0) , \tag{B.10}$$

after rearranging

$$F = \left(\gamma + \frac{c_1}{\Gamma_1}\right)(1 - S_0) + (\gamma_1 - \gamma)\, S_1 , \tag{B.11}$$

by using Equation (B.5) for $S_1$, (B.9) for $S_0$, and by rearranging,

$$F = \left[(\gamma_1 - \gamma)\, Y - \left(\gamma + \frac{c_1}{\Gamma_1}\right)\right]\left(\frac{1-X+Z}{1-X+Y}\right) - \left[(\gamma_1 - \gamma)\, Z - \left(\gamma + \frac{c_1}{\Gamma_1}\right)\right] . \tag{B.12}$$

Equation (B.12) reduces to

$$F = \frac{(Y - Z)\left[(\gamma_1 - \gamma)\,(1 - X) + \left(\gamma + \frac{c_1}{\Gamma_1}\right)\right]}{(1 - X + Y)} . \tag{B.13}$$

Substituting the values of X, Y, and Z into Equation (B.13) yields the general form of the adsorption equation of the assumed model:

$$F = a_1 \frac{\dfrac{(\gamma\gamma_1 + a\gamma - a\gamma_1)_{\Gamma_1^2}}{(\gamma\gamma_1 + a_1\gamma - a\gamma_1)} + \dfrac{(b\gamma_1 + \gamma c_1)_{\Gamma_1}}{(\gamma\gamma_1 + a_1\gamma - a\gamma_1)} + \dfrac{bc_1}{(\gamma\gamma_1 + a_1\gamma - a\gamma_1)}}{\Gamma_1^2 + \dfrac{(\gamma_1 b + \gamma b_1 + a_1 b + \gamma c_1 - a b_1)_{\Gamma_1}}{(\gamma\gamma_1 + a_1\gamma - a\gamma_1)} + \dfrac{(bb_1 + bc_1)}{(\gamma\gamma_1 + a_1\gamma - a\gamma_1)}} . \tag{B.14}$$

The coefficients of Equation (B.14) are obtained by fitting the data to a theoretical profile so that they are consistent with the assumptions made in the adsorption model. The simplest consistent form is obtained by letting $c_1 = \gamma_1 = 0$. With this simplification,

$$F = a_1 \frac{a\gamma\Gamma_1^2}{a_1\gamma\Gamma_1^2 + (\gamma b_1 + a_1 b - a b_1)\Gamma_1 + b b_1} . \tag{B.15}$$

By using the above assumptions, for the minimum angle of attack,

$$F_{\alpha_{min}} = .517 \frac{\Gamma_1^2}{\Gamma_1^2 + (3.23 \times 10^{13})\,\Gamma_1 + 2.00 \times 10^{26}} \quad . \tag{B.16}$$

and for the 90 deg angle of attack,

$$F_{90°} = \frac{\Gamma_1^2}{\Gamma_1^2 - (.528 \times 10^{13})\,\Gamma_1 + 6.89 \times 10^{26}} \quad . \tag{B.17}$$

## FIGURE CAPTIONS

Figure 1. The thermosphere probe in the clam shell nose cone.

Figure 2. Cross section of the quadrupole ion source and lens chamber with the electron beam trajectory.

Figure 3. Sample of the telemetry record obtained from the quadrupole.

Figure 4. (a) Maximum and minimum angle of attack between the thermosphere probe axis and the velocity vector versus time from launch.
(b) Expanded view of a section of Figure 4A.

Figure 5. Ion source nitrogen density versus flight time for minimum angle of attack, 90 deg angle of attack, and maximum angle of attack.

Figure 6. Ion source molecular oxygen density versus flight time for minimum angle of attack, 90 deg angle of attack, and maximum angle of attack.

Figure 7. Ion source atomic oxygen density versus flight time for minimum angle of attack, 90 deg angle of attack, and maximum angle of attack.

Figure 8. Simplified model of the geometry of the quadrupole ion source.

Figure 9. Computed molecular nitrogen density versus altitude for minimum angle of attack and 90 deg angle of attack assuming no thermal accommodation (curves A and B), and complete thermal accommodation (curves C and D).

Figure 10. Ambient molecular nitrogen density versus altitude obtained from the curves of Figure 9 by varying the coefficients $a_2$ and $a_3$ or $\epsilon$. The dashed line shows the nitrogen density profile obtained from the omegatron.

Figure 11. Computed molecular oxygen density versus altitude for minimum angle of attack and 90 deg angle of attack assuming no thermal accommodation (curves A and B), and complete thermal accommodation (curves C and D).

Figure 12. Ambient molecular oxygen density versus altitude, obtained from the curves of Figure 11 by varying the coefficients $a_2$ and $a_3$ or $\epsilon$.

Figure 13. Computed atomic oxygen density versus altitude for minimum angle of attack assuming (1) complete adsorption of particles striking the surface (curve A), (2) no adsorption and no thermal accommodation of particles striking the top deck (curve B), (3) no adsorption and complete thermal accommodation of particles striking the top deck (curve C). A theoretical profile computed by assuming diffusive and thermal equilibrium and by using the omegatron temperature is shown by the dashed line.

Figure 14. Computed atomic oxygen density versus altitude for 90 deg angle of attack assuming (1) complete adsorption of particles striking the surface (curve A), (2) no adsorption and no thermal accommodation of particles striking the top deck (curve B), (3) no adsorption and no thermal accommodation of particles striking the top deck (curve C). The two dashed lines each result from assuming diffusive and thermal equilibrium and from using the omegatron temperature. The top dashed line assumes complete

adsorption at 170 km. The bottom dashed line assumes complete accommodation and no adsorption at high altitudes.

Figure 15. Ambient atomic oxygen density versus altitude.

Figure 16. Ambient particle densities of molecular nitrogen, atomic and molecular oxygen versus altitude.

Figure 17. Ambient particle density ratios of atomic to molecular oxygen, atomic oxygen to molecular nitrogen, and of molecular oxygen to molecular nitrogen versus altitude.

Figure 18. Ambient temperature versus altitude. The dashed lines show the value of the CIRA 1965 models 3 and 4 for 1400 hours.

Figure 19. Total mass density of major constituents versus altitude. The dashed lines show the value of the CIRA 1965 models 3 and 4 for 1400 hours.

Table I. Final results of the quadrupole experiment showing number densities ($n_a(N_2)$, $n_a(O_2)$, $n_a(O)$), number density ratios ($O/O_2$, $O/N_2$, $O_2/N_2$), mass density of major constituents ($\rho$), and mean molecular weight of major constituents (M).